The Astrophysical Journal, 792:132 (14pp), 2014 September 10 doi:10.1088/0004-637X/792/2/132


# DISSOCIATIVE RECOMBINATION MEASUREMENTS OF $NH^+$ USING AN ION STORAGE RING

O. Novotný[1], M. Berg[2], D. Bing[2], H. Buhr[2], W. Geppert[3], M. Grieser[2], F. Grussie[2], C. Krantz[2], M. B. Mendes[2], C. Nordhorn[2], R. Repnow[2], D. Schwalm[2,4], B. Yang[2,5], A. Wolf[2], and D. W. Savin[1]
[1] Columbia Astrophysics Laboratory, Columbia University, New York, NY 10027, USA; oldrich.novotny@mpi-hd.mpg.de
[2] Max Planck Institute for Nuclear Physics, D-69117 Heidelberg, Germany
[3] Department of Physics, Stockholm University, AlbaNova, SE-106 91, Stockholm, Sweden
[4] Faculty of Physics, Weizmann Institute of Science, Rehovot 76100, Israel
[5] Institute of Modern Physics, Chinese Academy of Sciences, Lanzhou 730000, China
*Received 2014 May 20; accepted 2014 July 1; published 2014 August 26*

## ABSTRACT

We have investigated dissociative recombination (DR) of $NH^+$ with electrons using a merged beams configuration at the TSR heavy-ion storage ring located at the Max Planck Institute for Nuclear Physics in Heidelberg, Germany. We present our measured absolute merged-beams recombination rate coefficient for collision energies from 0 to 12 eV. From these data, we have extracted a cross section, which we have transformed to a plasma rate coefficient for the collisional plasma temperature range from $T_{\rm pl} = 10$ to 18,000 K. We show that the $NH^+$ DR rate coefficient data in current astrochemical models are underestimated by up to a factor of approximately nine. Our new data will result in predicted $NH^+$ abundances lower than those calculated by present models. This is in agreement with the sensitivity limits of all observations attempting to detect $NH^+$ in interstellar clouds.

*Key words:* astrochemistry – ISM: clouds – ISM: molecules – methods: laboratory: molecular – molecular data – molecular processes

## 1. INTRODUCTION

Unraveling the molecular evolution of the universe hinges, in part, on our understanding of nitrogen and the associated chemistry. Nitrogen is the fifth most cosmically abundant element (Asplund et al. 2009). Nitrogen-bearing species account for ∼35% of the molecules identified in space to date (Woon 2012) and can be found in a variety of space environments (e.g., Wyckoff et al. 1991; Vuitton et al. 2006; Hily-Blant et al. 2010; Persson et al. 2010).

In the cold ISM, such as in molecular clouds, the most abundant nitrogen-bearing species are expected to be N and $N_2$ (Langer & Graedel 1989). However, direct observation of these is difficult. Atomic N does not have any low-lying, fine-structure levels that can be populated at molecular cloud temperatures and $N_2$ lacks a dipole moment, which is needed to provide reasonably strong ro-vibrational transitions. Thus, observations of tracers such as NH, $NH_2$, $NH_3$, or $N_2H^+$ must be used to infer the N and $N_2$ abundances through chemical models.

Neutral nitrogen hydrides are widely seen in the ISM. Ammonia ($NH_3$) was first detected by Cheung et al. (1968). Later, $NH_2$ and NH were identified by van Dishoeck et al. (1993) and Meyer & Roth (1991), respectively. The observed abundances, however, do not match predictions from astrochemical models. In diffuse interstellar clouds, the observed abundance ratios for $NH/NH_3$ are ∼1.7 and, for $NH_3/H$, $\sim 3.2 \times 10^{-9}$. These cannot be simultaneously explained by existing chemical models. The models can fit either of the observed values, but then the other predicted ratio is a factor of 10 off from the observation (Persson et al. 2010). Similarly, in dark clouds the abundance ratio for $NH/NH_3$ is underpredicted by more than an order of magnitude (Hily-Blant et al. 2010). These discrepancies possibly originate from using incorrect reaction rate coefficients in the models.

Key to understanding the nitrogen chemical network are the simple nitrogen hydrides, both neutral and ionized (Pickles & Williams 1977; de Almeida & Singh 1982; Hily-Blant et al. 2010; Persson et al. 2010; Dislaire et al. 2012). In the gas-phase, cold ISM, these simple hydrides are generated primarily within the ammonia formation pathway. The reaction chain begins with $NH^+$ production through

$$N^+ + H_2 \rightarrow NH^+ + H. \quad (1)$$

Although this reaction is endoergic by ∼19 meV and also dependent on both the ortho versus para state of $H_2$ as well as on the fine-structure excitation of the $N^+$, for all permutations it still proceeds even at temperatures as low as 10 K (Dislaire et al. 2012; Zymak et al. 2013 and references therein). It has also been shown that $NH^+$ can then react with $H_2$ to form yet more complex nitrogen hydride ions via the series of reactions

$$NH^+ \xrightarrow{H_2} NH_2^+ \xrightarrow{H_2} NH_3^+ \xrightarrow{H_2} NH_4^+. \quad (2)$$

Dissociative recombination (DR) of any of the last three ions with electrons can form neutral nitrogen hydrides. Ammonia is formed by DR of $NH_4^+$ via the product channel

$$e^- + NH_4^+ \rightarrow NH_3 + H. \quad (3)$$

Reactions (2) and (3) indicate that $NH^+$ is a key molecule for gas-phase nitrogen chemistry, and several attempts have been made to detect it in the ISM (Snow 1979; Polehampton et al. 2007; Hily-Blant et al. 2010; Persson et al. 2010, 2012). None, however, have been successful. Our understanding of the role played by $NH^+$ in forming more complex nitrogen hydrides thus relies entirely on the accuracy of the relevant formation and destruction rate coefficients needed for the astrochemical models.

An important destruction channel for $NH^+$ is DR through

$$e^- + NH^+ \rightarrow N + H. \quad (4)$$

This reaction was previously investigated by McGowan et al. (1979) in a single-pass merged-beams experiment. In their measurement, the ions did not have time to relax and are

expected to have been highly ro-vibrationally and possibly also electronically excited. Other experimental studies show that the DR rate coefficient can depend significantly on the internal excitation of the ions (e.g., Amitay et al. 1998; McCall et al. 2004). Therefore, the results of McGowan et al. are unlikely to be applicable to astrochemical models of the cold ISM where the ions are expected to be in their vibrational ground state. Additionally, the lowest collision energies investigated by McGowan et al. correspond to a collisional plasma temperature of ∼100 K; but modeling the cold ISM requires rate coefficients down to temperatures of ∼10 K. Extrapolating their results down to these temperatures introduces additional uncertainty into the models. Moreover, the original data of McGowan et al. were later corrected for an erroneous scaling used in the data analysis. The revised rate coefficient is smaller by a factor of ∼2.5 (Mitchell 1990; J. B. A. Mitchell 2012, private communication). Unfortunately, databases used by astrochemical models mix the original and the corrected rate coefficient values (e.g., Wakelam et al. 2012; McElroy et al. 2013).

In order to help improve our understanding of the nitrogen astrochemistry, we have carried out DR measurements for $NH^+$. The rest of this paper is organized as follows. The possible pathways for DR of $NH^+$ are discussed in Section 2. The experimental setup, measurement method, and data analysis are described in Section 3. In Section 4, we present the resulting merged-beams DR rate coefficient for $NH^+$, extract a DR cross section, and subsequently derive a Maxwellian plasma DR rate coefficient. We discuss our results and their implications for astrochemistry in Section 5. A summary is given in Section 6. In addition, to the present study, we have investigated the $NH^+$ DR at high collision energies. These complementary results were published by Yang et al. (2014).

## 2. DR PATHWAYS FOR $NH^+$

In DR, the incident electron is first captured into a doubly excited state of the neutral molecule (Bates 1950; Bardsley 1968; Larsson & Orel 2008). If the potential surface of such a state is repulsive, the neutral system formed can directly dissociate into neutral products. Alternatively, if the electron is captured to a bound state it can subsequently predissociate by coupling to a neutral repulsive state. These two basic pathways are referred to as direct and indirect DR, respectively. In both cases, the overlap within the Frank–Condon region between the initial ionic state and the intermediate neutral excited state defines the shape of the DR cross section versus the electron–ion collision energy, $E$. A more detailed description of the various DR pathways is given in Larsson & Orel (2008). Additionally, the impact of molecular structure on the energy dependence of the DR cross section has been described by Wolf et al. (2011) and Novotný et al. (2013). In this section, we discuss the molecular structure of both $NH^+$ and NH, and review some of the expected energy dependence for DR of $NH^+$.

The structure of NH and $NH^+$ has been studied both spectroscopically and theoretically (e.g., Colin & Douglas 1968; Wilson & Richards 1978; Goldfield & Kirby 1987; Kawaguchi & Amano 1988; Colin 1989; Clement et al. 1992; Palmieri et al. 1996; Amero & Vázquez 2005; Owono Owono et al. 2007; Hübers et al. 2009; Beloy et al. 2011). To the best of our knowledge, however, no potential energy curves have been published for the repulsive doubly excited NH states. Nevertheless, these states are expected to form various Rydberg series with each series converging to a single repulsive ionic core state as the principle quantum number, $n$, of the captured electron goes to $\infty$. The two $NH^+$ repulsive ionic core states relevant for this study are the $2\,^2\Pi$ and $2\,^4\Sigma^-$, with vertical excitation energies in the Franck–Condon region of ∼7.7 eV and ∼10.5 eV, respectively (Amero & Vázquez 2005; a summary of known NH and $NH^+$ potential energy curves relevant for $NH^+$ DR can be found in Yang et al. 2014). The Rydberg series of neutral doubly excited repulsive states converging to these thresholds can lead to direct DR. The nonresonant nature of the transition between the initial ionic state and the repulsive neutral state typically results in broad features in the DR energy spectrum.

Indirect DR proceeds via neutral bound states. These can also be grouped into different Rydberg series, each converging to a particular ionic core level. The excitation energy of each ionic core forms an upper limit for a given series of indirect DR resonances. Individual resonances are often experimentally unresolvable. However, the series limits may appear more clearly in the measured cross section versus collision energy. If the neutral Rydberg states contribute significantly to DR, then the DR signal will decrease as the collision energy scans over the ionic threshold. On the other hand, the neutral Rydberg states may also lead to additional autoionization channels or can be an initial step for various other reactions, such as dissociative excitation or ion-pair formation, which compete with DR. This can lead to a reduction in DR from other channels (e.g., direct DR) through the given neutral Rydberg state. In an extreme case, such DR reduction through Rydberg states may appear as a DR increases above the ionic limit. From the available data on the $NH^+$ structure, we cannot predict which of these cases will dominate for particular Rydberg series.

For indirect DR, there are a number of different $NH^+$ ionic core thresholds that can be relevant to DR at the lowest collision energies. These thresholds include the $X\,^2\Pi$ excited rotational $J$ levels, fine structure excitation to the $X\,^2\Pi_{3/2}$ level by ∼13 meV, and the ∼42 meV excitation to the $a\,^4\Sigma^-$ electronic state (Hübers et al. 2009). The vibrational, $v$, levels of the $NH^+$ $X\,^2\Pi$ and $a\,^4\Sigma^-$ states can also play a role. The level spacing for these two vibrational series is approximately 0.38 eV and 0.33 eV, respectively (Amero & Vázquez 2005). The next higher lying $NH^+$ bound electronic states are the $A\,^2\Sigma^-$, $B\,^2\Delta$, and $C\,^2\Sigma^+$. The corresponding thresholds for indirect DR from ground-state $NH^+$ to the lowest vibrational levels of these electronic states may appear at $E \approx 2.7$ eV, 2.8 eV, and 4.3 eV, respectively (Colin & Douglas 1968). Note that neutral resonances corresponding to electron capture into Rydberg levels attached to these electronic state thresholds extend several electron volts below these thresholds and can hence be important over a large range of electron collision energies.

DR of $NH^+$ is exothermic. The amount of available energy constrains both the maximum internal excitation of the products and also the number of possible dissociation pathways. The DR cross section may increase above the threshold for forming excited atomic products as a result of the opening up of new dissociation channels. To evaluate the exothermicity for DR of $NH^+$, we briefly review the relevant thermochemical data. The $NH^+$ ground state $X\,^2\Pi_{1/2}(v = 0, J = 1/2)$ lies $3.524 \pm 0.003$ eV below the $N + H^+$ dissociation limit (Marquette et al. 1988). The ground state N + H products lie energetically lower by the hydrogen ionization energy of 13.598 eV (Linstrom & Mallard 2013). From these values, we obtain an $NH^+$ DR exothermicity at $E = 0$ eV of $10.074 \pm 0.003$ eV. This energy is shared between the product electronic excitation and the kinetic energy released (KER) in the DR process. At $E = 0$ eV, the exothermicity is insufficient to excite the H atom and it

**Table 1**
Product Excitation Channels for DR of Ground State $NH^+$ at an Electron–Ion Collision Energy of $E = 0$ eV

| ID | H State | N State | KER (eV) |
|---|---|---|---|
| 1 | $1s\ ^2S_{1/2}$ | $2s^22p^3\ ^4S^o_{3/2}$ | 10.074 |
| 2 | $1s\ ^2S_{1/2}$ | $2s^22p^3\ ^2D^o_{5/2}$ | 7.690 |
| 3 | $1s\ ^2S_{1/2}$ | $2s^22p^3\ ^2P^o_{1/2}$ | 6.498 |
| 4 | $2p\ ^2P^o_{1/2}$ | $2s^22p^3\ ^4S^o_{3/2}$ | −0.125 |
| | $2s\ ^2S_{1/2}$ | $2s^22p^3\ ^4S^o_{3/2}$ | −0.125 |
| 5 | $1s\ ^2S_{1/2}$ | $2s^22p^2(^3P)3s\ ^4P_{1/2}$ | −0.252 |
| 6 | $1s\ ^2S_{1/2}$ | $2s^22p^2(^3P)3s\ ^2P_{1/2}$ | −0.606 |
| 7 | $1s\ ^2S_{1/2}$ | $2s^22p^4\ ^4P_{5/2}$ | −0.850 |
| 8 | $1s\ ^2S_{1/2}$ | $2s^22p^2(^3P)3p\ ^2S^o_{1/2}$ | −1.529 |

**Notes.** For each electronic state of H or N, only the lowest fine-structure level is listed. The fine-structure splitting for the omitted levels is less than 10 meV each. Negative KER values indicate channels energetically closed at $E = 0$ eV, which become energetically allowed for $E \geqslant -$KER. Channel 4 has two possible hydrogen configurations that differ energetically by less than 5 $\mu$eV.

is produced in the $^2S_{1/2}$ ground state. On the other hand, for nitrogen, there are three electronic terms available, namely the $^4S^o$ ground term and the excited $^2D^o$ and $^2P^o$ terms, with KERs of 10.074 eV, 7.690 eV, and 6.498 eV, respectively. Additional channels open at higher collision energies. The channels most important for discussing our $NH^+$ results open at collision energies below ∼1.6 eV. The channels relevant for this energy range are listed in Table 1. Channels that play a role at higher energies can be readily obtained from the atomic data of Ralchenko et al. (2011). It should be emphasized that all exothermicities are given for $NH^+$ being in its ground state. Any internal excitation of the $NH^+$ results in an increase in the exothermicity of the reaction. This internal excitation shifts the collision energy thresholds for opening the product channels with indices ID $\geqslant$ 4 (see Table 1) to correspondingly lower values (less negative KER in Table 1). Experimentally, we expect internal excitation to result in a smoothing with $E$ of the threshold behavior. This is a consequence of the stored ions coming into thermal equilibrium with the ambient 300 K temperature of TSR, resulting in a range of rotational levels being populated.

There are other electron-induced processes that could compete with DR, and thus reduce the DR signal. For the case of $NH^+$, these competing processes are all endothermic. One of these is ion-pair formation, which can yield $N^+ + H^-$ at energy above ∼3.7 eV. The complementary channel $N^- + H^+$ is not expected to exist due to instability of $N^-$ (Linstrom & Mallard 2013). Another electron-driven process is dissociative excitation (DE) forming N + $H^+$ or $N^+$ + H. These reactions are endothermic by ∼3.5 eV and ∼4.5 eV, respectively.

## 3. EXPERIMENTAL

### 3.1. Setup

Data were collected in 2010 July using the TSR storage ring located at the Max Planck Institute for Nuclear Physics (MPIK) in Heidelberg, Germany. Details on various aspects of this merged-beams experimental setup have been described in more detail by Amitay et al. (1996a), Wolf (1999), and Novotný et al. (2013). Here, we discuss only those aspects specific to this study.

To generate the $NH^+$ ion beam, we first produced $NH_3^-$ in a cesium sputtering source with a molybdenum target and ammonia as the parent gas. The negative ions were accelerated and then directed through a nitrogen gas stripping curtain. The resulting $NH^+$ ions were further accelerated to a final energy of $E_i \approx 6.2$ MeV and injected into the storage ring. Typical stored ion currents were ∼0.3 nA during data acquisition.

The stored ion beam was merged with two nearly monoenergetic electron beams, dubbed the Target (Sprenger et al. 2004) and the Cooler (Steck et al. 1990). Starting after ion injection at time $t = 0$, both electron beams were velocity matched to the ions until $t = 6$ s. During this time, elastic collisions of the ions with the low energy spread electron beams transferred energy from the recirculating ions to the single pass electrons, a process known as electron cooling (Poth 1990). This reduced the energy spread of the ions and resulted in a narrow ion beam diameter (<1 mm). Data were collected from $t = 6$ s to $t = 16.5$ s. This was then followed by ion injection, and the cycle repeated.

The energy spread of each electron beam is critical for the energy resolution of the experiment. The energy distribution is parameterized by the effective temperatures, $T_\perp$ and $T_{||}$, respectively perpendicular and parallel to the bulk electron beam velocity. The Target electron beam was produced using a photocathode in transmission mode (Orlov et al. 2004, 2009) and expanded adiabatically by a factor of 20. For these conditions, we expect $k_B T_\perp^T = 1.65 \pm 0.35$ meV and $k_B T_{||}^T = 25^{+45}_{-5}$ $\mu$eV (Novotný et al. 2013), where $k_B$ is the Boltzmann constant. Here, and throughout, all uncertainties are quoted at an estimated $1\sigma$ statistical confidence level. The Cooler uses a thermionic emission cathode and expansion factor of 9.6. The corresponding electron beam temperatures are $k_B T_{||}^C \approx 180$ $\mu$eV and $k_B T_\perp^C \approx 13.5$ meV (Lestinsky et al. 2008).

After the cooling phase, the Target electron beam was used as a probe to measure DR over a range of electron–ion center-of-mass collision energies. This was accomplished by varying the laboratory energy of the Target. While this was happening, the Cooler beam remained velocity matched with the ions at all times. In this way, the ion beam was continuously cooled and did not expand in size or shift in energy as the Target beam was detuned. The Target and Cooler were operated with typical electron beam densities of $n_e^T \approx 2.7 \times 10^6$ cm$^{-3}$ and $n_e^C \approx 2.5 \times 10^7$ cm$^{-3}$, respectively. Neutral DR products generated in the Target were not deflected by the first dipole magnet downstream of the Target and continued ballistically until they hit a detector. The detected signals provided the event count rates.

### 3.2. $NH^+$ Internal Excitation

Ions produced by stripping are initially expected to possess electronic, vibrational, rotational, and fine-structure excitation. We estimate that radiative relaxation removes most of the $NH^+$ internal excitation during the 6 s of electron cooling, resulting in a parent ion population far closer to astrophysical conditions than that which was achievable in the single pass results of McGowan et al. (1979). Below the first $NH^+$ dissociation limit lie the $a\ ^4\Sigma^-$, $A\ ^2\Sigma^-$, and $B\ ^2\Delta$ excited electronic states. The measurements of Brzozowski et al. (1974) yielded decay times for the $A\ ^2\Sigma^-$ and $B\ ^2\Delta$ states of ∼1 $\mu$s. Thus, these states are expected to have fully decayed before the onset of data acquisition. To the best of our knowledge, there have been

no such investigations into the radiative lifetime of the $a\,^4\Sigma^-$ symmetry. Moreover, even if this state quickly relaxes into thermal equilibrium with the ∼300 K vacuum chamber, the expected Boltzmann distribution indicates that ∼15% of the $NH^+$ will be in the $a\,^4\Sigma^-$ state.

We are not aware of any theoretical or experimental investigations into radiative relaxation of the $NH^+$ ro-vibrational levels and have therefore calculated them ourselves. We predict that all of the ions relax to their $v = 0$ level and that the rotational excitation comes into equilibrium with the ∼300 K blackbody radiation of the vacuum chamber during the initial electron cooling phase. To model this, we have calculated the ro-vibrational radiative lifetimes of $X\,^2\Pi_{1/2}$ for levels ranging from $v = 1$ to $v = 5$ and from $J = 3/2$ to $J = 19/2$. Higher levels are calculated to decay so rapidly that they are irrelevant for the model. Our approach uses a method similar to that of Amitay et al. (1994). The dipole moment for $NH^+$ was taken from Cheng et al. (2007). With this as a guide, we have generated a radiative relaxation model using the calculated spontaneous radiative decay lifetimes, while also accounting for stimulated emission and absorption by the 300 K blackbody radiation. For the initial rotational excitation, we have taken a Boltzmann distribution at a temperature of 8000 K. This is approximately the excitation temperature derived in a similar DR experiment on $CF^+$ (Novotný et al. 2009). After the initial 6 s of ion storage, the model predicts all vibrational levels decayed to $v = 0$. The remaining average rotational excitation energy exceeds the 300 K equilibrium by only 12%. The excitation energy averaged over the ion population during the measurement window, from $t = 6.0$ to 16.5 s, exceeds room temperature excitation by only 4.6%. This predicted level of excitation might be overestimated due to the omission of spin–orbit coupling and coupling to the $a\,^4\Sigma^-$ state, both of which may result in extra decay pathways. The model also does not take into account additional acceleration of the rotational cooling from super-elastic ion collisions with electrons (e.g., Shafir et al. 2009).

The final excitation to consider is the fine structure splitting $X\,^2\Pi_{1/2-3/2}$. This is not expected to relax during ion storage. We are unaware of any published lifetime estimates for this transition. Moreover, the excitation energy of ∼13 meV is well within the energies accessible by the ∼300 K ambient radiation. Taking into account the Boltzmann distribution at 300 K for all the rotational levels in the $X\,^2\Pi_{1/2}$ and $X\,^2\Pi_{3/2}$ fine-structure levels (Kawaguchi & Amano 1988), we predict that the two fine-structure groups are statistically populated by ∼67% and ∼33%, respectively.

### 3.3. Measurements

During the data acquisition phase of each injection cycle, the Target electron beam energy was stepped over a repeating set of three different energies. For the first step, cooling, the Target electrons were velocity matched to the ions at an electron energy of $E_{\rm cool} = 226.74$ eV in the laboratory frame. Although the Cooler beam continuously cooled the ions, the much narrower energy spread of the Target beam provided even stronger cooling during this step. This helped to maintain a stable phase-space spread of the ions during storage.

In the next step, measurement, the Target beam was set to a mean energy of $E_{\rm meas}$ in the laboratory frame. The center-of-mass collision energy, the so-called detuning energy, $E_{\rm d}$, can be calculated nonrelativistically from the mean electron and ion beam velocities, or from corresponding laboratory-frame ion beam energies as

$$E_{\rm d} = (\sqrt{E_{\rm meas}} - \sqrt{E_{\rm cool}})^2. \quad (5)$$

The count rate at the detector during this step was used to obtain the merged-beam DR rate coefficient at the calculated $E_{\rm d}$. The measurement energy, and hence detuning energy, was changed for each injection cycle.

In the last step, reference, the Target beam energy was set to a detuning energy $E_{\rm d}^{\rm ref} \approx 29$ meV. This reference energy was identical for all injection cycles. The detector count rate during this step was used to monitor the ion beam intensity.

The laboratory frame electron beam energies for each step were obtained from the Target cathode voltage, which was then corrected for space-charge effects (Kilgus et al. 1992). The power supply providing the cathode voltage requires a short time to equilibrate. Thus, to ensure stable conditions during data acquisition at each step, we add 5 ms of settling time between setting the new cathode voltage and the start of the corresponding step. Excluding this settling time, the dwell times at the cooling, measurement, and reference steps were 40 ms, 30 ms, and 30 ms, respectively.

The count rate of the DR events was measured using a $10 \times 10$ cm$^2$ energy sensitive Si surface-barrier detector located ∼12 m downstream of the Target. For each DR event, the N and H fragments arrive at the detector with a time difference of only a few nanoseconds. Such a small delay cannot be distinguished by the detector, and hence only a single pulse is detected for each DR event, representing the total kinetic energy of the fragments.

Typically, both fragments reached the detector and the measured total kinetic energy corresponds to the original ion beam energy. However, DR of $NH^+$ can release several eV in kinetic energy (see Table 1). Such a kick in the direction perpendicular to the parent ion beam can sufficiently deflect the light H fragments so that they miss the active area of the detector. On the other hand, the kinetic energy released has little effect on the heavier N fragments. They remain confined to a narrow cone, which is fully enclosed by the detector. The DR signal is therefore a sum of detections of both fragments and detections of only the N fragment.

A number of background processes can mimic our signal and must be accounted for. For example, electron-ion collisions can result in DE producing N and $H^+$ fragments. The threshold for this DE channel is ∼3.5 eV. Thus, for $E_{\rm d}$ below this, to determine the DR signal we can use events with kinetic energies corresponding to capturing both fragments (N+H) and also those detecting only the N fragments. At higher energies, however, DE events could contaminate the DR data. Hence, above ∼3.5 eV, we used only events where both N and H reached the detector. These data then need to be adjusted to account for those DR events where the H fragment does not hit the detector due to the detector size. This correction was measured independently using a position sensitive detector (Buhr et al. 2010; B. Yang et al., in preparation). The resulting rescaling of the DR signal was less than 7% over the energy range studied.

The DR signal was also contaminated by reaction products from various collisions of the ions with the residual gas. Dissociative charge transfer produces neutral N and H fragments. Collision-induced dissociation can produce either N and $H^+$ fragments or $N^+$ and H fragments. In all of these cases, the resulting N + H and N events on the neutral-fragment detector can be misinterpreted as DR and need to be accounted for. To do this, we used the fact that the rate of these background events, $R_{\rm BG}$, scales with the ion beam intensity and with the

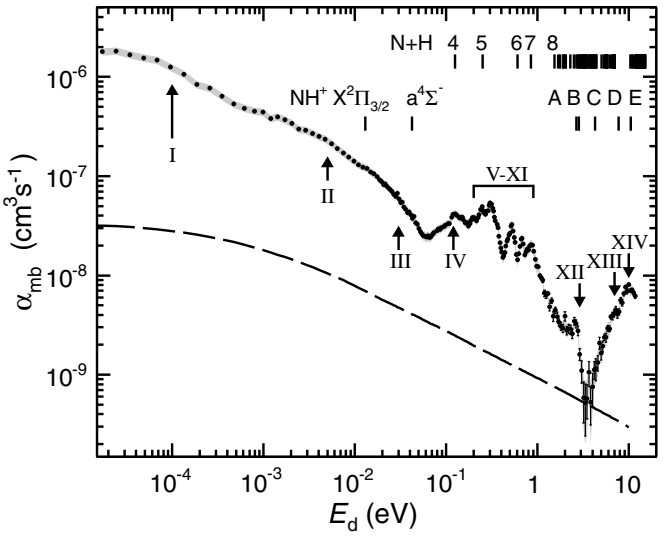


**Figure 1.** Experimental merged-beams rate coefficient, $\alpha_{mb}$, for DR of $NH^+$. The filled circles show the data and the error bars indicate the $1\sigma$ statistical confidence level. The total $1\sigma$ systematic error is marked in gray. The long dashed line illustrates the shape of a merged-beams rate coefficient expected for a direct DR process, i.e., for a cross section $\sigma(E) \propto E^{-1}$, and is arbitrarily scaled on the vertical axis. The uppermost series of vertical lines marks the openings of various $NH^+$ DR product excitation channels. The energy thresholds are given for $NH^+$ in its ground state. The channel ID numbers are given in Table 1. The vertical lines in the second row mark the excitation energies for various $NH^+$ states. The $X\,^2\Pi_{3/2}$ and $a\,^4\Sigma^-$ levels are labeled directly in the figure. The labels A, B, C, D, and E correspond to $A\,^2\Sigma^-$, $B\,^2\Delta$, $C\,^2\Sigma^+$, $2\,^2\Pi$ and $2\,^4\Sigma^-$ states, respectively. Roman numbers label various features in the DR spectrum, which are discussed in the text.

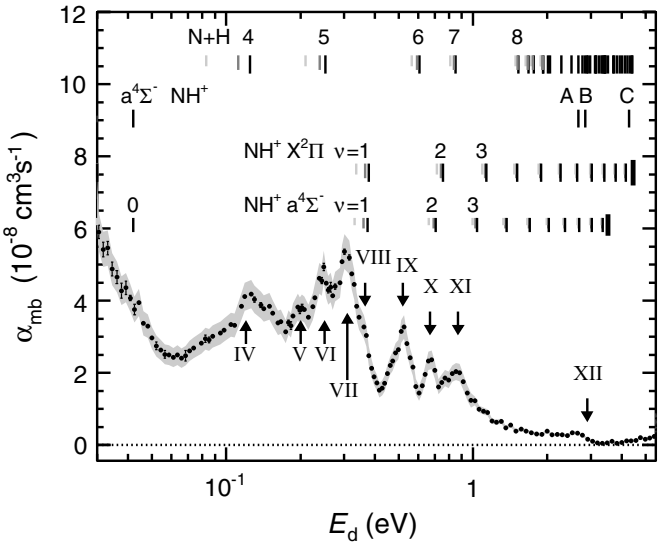


**Figure 2.** Same as Figure 1, but plotted for $E_d \approx 0.04$–$5.0$ eV on a lin–log scale. Additionally, we have extended the number of plotted energy thresholds. The first row of black vertical lines marks openings of $NH^+$ DR product excitation channels for $NH^+$ in its ground state. The shorter dark-gray lines then assume $NH^+$ initially in the $X\,^2\Pi_{3/2}$ excited fine structure level. The shorter light-gray lines assume $NH^+$ initially in the $a\,^4\Sigma^-(v = 0)$ state. The vertical lines in the second row mark the excitation energies for various $NH^+$ states. The third and fourth series of vertical lines label vibrational thresholds for $NH^+$ $X\,^2\Pi$ and $a\,^4\Sigma^-$, respectively. The black, dark-gray, and light-gray encoding is identical to the first row of vertical lines. Thick lines at the end of each vibrational series mark the respective $NH^+$ dissociation limits.

residual gas pressure, but—in contrast to DR—it does not depend on the electron density. Thus, any signal that does not depend on the electron beam density can be used as a proxy for the total DR background rate at the neutral-fragment detector induced by residual gas collisions. Here, we use the signal from $N^+$ fragments produced in collision-induced dissociation to monitor the relative ion beam intensity. For this, we employ a detector located in the first dipole magnet downstream the Target (Lestinsky 2007). This detector was positioned such that only $N^+$ fragments originating in the Target were deflected onto its active area. We used only the data from the reference step, which is at an energy below the threshold for DE forming $N^+ + H$. A scaling factor, $\xi$, is needed to match the $N^+$ count rate, $R_{N^+}$, to the background count rate, $R_{BG}$, so that $R_{BG} = \xi R_{N^+}$.

We determined $\xi$ independently using a special measurement scheme. After ion injection and the cooling phase, we switched off the Target electron beam. The ion beam was still cooled by the Cooler. With the Target off, the count rate at the neutral fragment detector originated only from residual gas-induced reactions and was thus equal to $R_{BG}$. Simultaneously, we also acquired the $R_{N^+}$ signal. The scaling factor, $\xi$, was simply obtained by comparing $R_{BG}$ to $R_{N^+}$ at the same storage times.

We determined the measured merged-beams DR rate coefficient $\alpha_{mb}(E_d)$ by normalizing the recorded DR signal by the electron density and ion number (e.g., Amitay et al. 1996a). The electron beam density can be determined from the measured electron beam current, energy, and geometry (Sprenger et al. 2004). The number of interacting ions can be calculated from the ion beam current. However, the typical stored $NH^+$ beam current was only a few nA. This is several orders of magnitude lower than what can be measured directly using the available DC current transformer (Unser 1981). Hence, we first determined a relative DR rate coefficient versus $E_d$ using the $R_{N^+}$ signal as a relative proxy for the ion beam current. We then scaled the whole curve to match the absolute rate coefficient value determined at $E_d = 0$ eV using an independent measurement technique based on comparing ion beam decay rates with and without the electron beam present in the interaction zone (Novotný et al. 2012).

### 3.4. Generating a DR Cross Section and a Plasma DR Recombination Rate Coefficient

In order to enable researchers to use our storage ring data in astrochemical models, we have converted the measured merged-beams DR rate coefficient into a plasma DR rate coefficient. The transformation is a two step process. First, the experimental collision energy distribution is deconvolved from $\alpha_{mb}(E_d)$ to obtain a cross section, $\sigma(E)$, as a function of collision energy $E$. In the second step, the cross section is convolved with a Maxwell–Boltzmann distribution to generate a plasma rate coefficient, $\alpha_{pl}(T_{pl})$, at the required collisional plasma temperature, $T_{pl}$. Here, $T_{pl}$ reflects the collisional velocity spread in a plasma at given temperature, but not the internal excitation of the ions. We have recently developed a novel method for converting $\alpha_{mb}(E_d)$ to $\sigma(E)$ and subsequently into $\alpha_{pl}(T_{pl})$. The procedure also allows for propagating statistical and systematic uncertainties. The method is described in detail by Novotný et al. (2013).

## 4. RESULTS

### 4.1. Merged-Beams Recombination Rate Coefficient

Figures 1 and 2 present our merged-beams rate coefficient for DR of $NH^+$. In Figure 1, we display the data on a log–log scale for the measured detuning energies $E_d = 15\ \mu$eV to 12 eV.

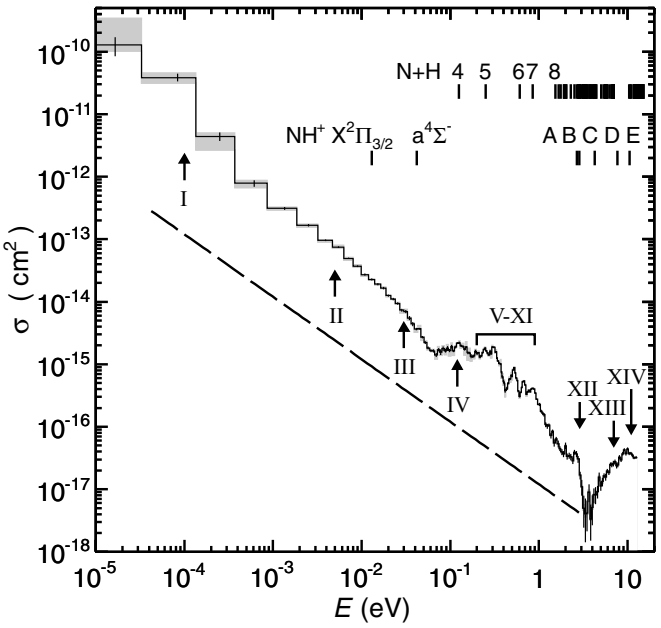


**Figure 3.** DR cross section for $NH^+$ is shown by the solid-line histogram. The lower edge of the left-most energy bin at $E = 0$ eV is not shown here. The vertical error bars describe the statistical uncertainty propagated from $\alpha_{mb}$ and potential numerical instabilities from the conversion procedure (for more details see Novotný et al. 2013). The gray error bands show the error originating from uncertainties in $k_B T_\perp^T$ and $k_B T_\parallel^T$. The long-dashed line illustrates the shape of the merged-beams rate coefficient expected for a direct DR process, i.e., $\sigma(E) \propto E^{-1}$. The curve is arbitrarily scaled on the vertical axis. The vertical lines and labels are identical to Figure 1.

These data are also given in tabular form in Table 2 . In Figure 2, we zoom in on the most pronounced rate coefficient structures in the detuning energy range from $E_d = 40$ meV to 5 eV and plot the data on a lin–log scale.

The systematic uncertainty in the measured $\alpha_{mb}$ has several important components. The uncertainties from the ion beam storage lifetime measurements, and from the electron density, dominate the 8.4% uncertainty on the absolute scaling of $\alpha_{mb}$. This value is independent of $E_d$. Another source of error is the background subtraction factor, $\xi$. At energies $E_d < 0.01$ eV, the corresponding uncertainty propagated to $\alpha_{mb}$ amounts to $\lesssim$1%. As the collision energy increases, the uncertainties are ∼5%, ∼10%, ∼50%, and ∼7% at $E_d = 0.1$ eV, 1.5 eV, 3.5 eV, and 10 eV, respectively. The energy dependence of the uncertainty is due to a decrease in DR up to 3.5 eV followed by an increase going to 10 eV, while the background stays constant. At $E_d > 3.5$ eV, an additional error originates from correcting for geometrical detector losses. We estimate this uncertainty to be less than 1%. The total systematic error is then $\lesssim$8.5%, ∼10%, ∼13%, ∼50%, and ∼11% at $E_d \lesssim 0.01$ eV as well as $E_d = 0.1$ eV, 1.5 eV, 3.5 eV, and 10 eV, respectively.

For each data point in $\alpha_{mb}$, the statistical uncertainty is given by the counting statistics from the number of signal and background counts. This error amounts to $\lesssim$4%, ∼10%, ∼50%, and ∼8% at $E_d \lesssim 1$ eV as well as $E_d = 1.5$ eV, 3.5 eV, and 10 eV, respectively.

### 4.2. Recombination Cross Section

We have converted the experimental DR rate coefficient $\alpha_{mb}$ to a cross section $\sigma$. The result is plotted in Figure 3. These data are also given in tabular form in Table 3. The lower edge

**Table 2**
Experimental Merged-beams Rate Coefficient $\alpha_{mb}$ for DR of $NH^+$

| $E_d$ (eV) | $\alpha_{mb}$ ($cm^3\ s^{-1}$) | Statistical Error ($cm^3\ s^{-1}$) |
|---|---|---|
| 1.71(−5) | 1.79(−6) | 6.63(−8) |
| 2.43(−5) | 1.82(−6) | 7.88(−8) |
| 3.43(−5) | 1.67(−6) | 5.50(−8) |
| 4.85(−5) | 1.55(−6) | 5.68(−8) |
| 6.83(−5) | 1.47(−6) | 6.60(−8) |
| 9.60(−5) | 1.25(−6) | 3.98(−8) |
| 1.34(−4) | 1.06(−6) | 3.11(−8) |
| 1.87(−4) | 8.38(−7) | 3.39(−8) |
| 2.57(−4) | 7.69(−7) | 2.96(−8) |
| 3.50(−4) | 6.36(−7) | 1.98(−8) |
| 4.70(−4) | 5.32(−7) | 1.52(−8) |
| 6.18(−4) | 4.83(−7) | 1.39(−8) |
| 7.92(−4) | 4.52(−7) | 1.30(−8) |
| 9.85(−4) | 4.41(−7) | 1.46(−8) |
| 1.19(−3) | 3.79(−7) | 1.16(−8) |
| 1.43(−3) | 3.95(−7) | 1.91(−8) |
| 1.71(−3) | 3.69(−7) | 9.75(−9) |
| 2.04(−3) | 3.40(−7) | 9.53(−9) |
| 2.43(−3) | 2.98(−7) | 8.33(−9) |
| 2.89(−3) | 2.91(−7) | 7.57(−9) |
| 3.42(−3) | 2.69(−7) | 4.46(−9) |
| 4.04(−3) | 2.51(−7) | 2.38(−9) |
| 4.75(−3) | 2.36(−7) | 2.92(−9) |
| 5.55(−3) | 2.13(−7) | 1.97(−9) |
| 6.45(−3) | 1.90(−7) | 1.89(−9) |
| 7.45(−3) | 1.71(−7) | 1.81(−9) |
| 8.55(−3) | 1.55(−7) | 1.80(−9) |
| 9.73(−3) | 1.42(−7) | 1.70(−9) |
| 1.10(−2) | 1.30(−7) | 1.77(−9) |
| 1.23(−2) | 1.24(−7) | 1.76(−9) |
| 1.36(−2) | 1.20(−7) | 1.79(−9) |
| 1.49(−2) | 1.10(−7) | 1.66(−9) |
| 1.62(−2) | 1.06(−7) | 1.93(−9) |
| 1.74(−2) | 9.92(−8) | 1.96(−9) |
| 1.86(−2) | 9.17(−8) | 1.92(−9) |
| 1.96(−2) | 8.82(−8) | 1.93(−9) |
| 2.06(−2) | 8.24(−8) | 1.84(−9) |
| 2.15(−2) | 8.40(−8) | 2.25(−9) |
| 2.25(−2) | 7.93(−8) | 1.59(−9) |
| 2.35(−2) | 7.57(−8) | 1.55(−9) |
| 2.45(−2) | 7.27(−8) | 2.10(−9) |
| 2.56(−2) | 7.01(−8) | 1.54(−9) |
| 2.67(−2) | 6.53(−8) | 1.49(−9) |
| 2.79(−2) | 6.27(−8) | 1.53(−9) |
| 2.91(−2) | 6.71(−8) | 2.68(−9) |
| 3.04(−2) | 5.91(−8) | 1.87(−9) |
| 3.17(−2) | 5.42(−8) | 2.02(−9) |
| 3.31(−2) | 5.46(−8) | 1.85(−9) |
| 3.45(−2) | 4.88(−8) | 1.94(−9) |
| 3.60(−2) | 4.66(−8) | 1.77(−9) |
| 3.76(−2) | 4.28(−8) | 2.07(−9) |
| 3.92(−2) | 4.36(−8) | 1.82(−9) |
| 4.08(−2) | 4.08(−8) | 7.19(−10) |
| 4.25(−2) | 3.75(−8) | 1.46(−9) |
| 4.43(−2) | 3.95(−8) | 6.27(−10) |
| 4.62(−2) | 3.38(−8) | 6.79(−10) |
| 4.81(−2) | 3.30(−8) | 6.40(−10) |
| 5.01(−2) | 2.97(−8) | 5.24(−10) |
| 5.21(−2) | 2.75(−8) | 1.07(−9) |
| 5.42(−2) | 2.63(−8) | 4.47(−10) |
| 5.64(−2) | 2.51(−8) | 1.08(−9) |
| 5.86(−2) | 2.49(−8) | 5.02(−10) |
| 6.10(−2) | 2.43(−8) | 5.84(−10) |
| 6.34(−2) | 2.49(−8) | 6.04(−10) |
| 6.58(−2) | 2.41(−8) | 4.46(−10) |

**Table 2**
(Continued)

| $E_d$ (eV) | $\alpha_{mb}$ ($cm^3\ s^{-1}$) | Statistical Error ($cm^3\ s^{-1}$) |
|---|---|---|
| 6.84(−2) | 2.48(−8) | 1.44(−9) |
| 7.10(−2) | 2.61(−8) | 6.10(−10) |
| 7.37(−2) | 2.70(−8) | 5.51(−10) |
| 7.93(−2) | 2.83(−8) | 6.14(−10) |
| 8.22(−2) | 2.95(−8) | 9.95(−10) |
| 8.52(−2) | 2.92(−8) | 7.95(−10) |
| 8.83(−2) | 3.01(−8) | 5.90(−10) |
| 9.46(−2) | 3.11(−8) | 6.15(−10) |
| 9.79(−2) | 3.19(−8) | 6.21(−10) |
| 1.05(−1) | 3.34(−8) | 6.37(−10) |
| 1.08(−1) | 3.32(−8) | 6.02(−10) |
| 1.15(−1) | 3.85(−8) | 6.33(−10) |
| 1.19(−1) | 4.11(−8) | 6.61(−10) |
| 1.26(−1) | 4.18(−8) | 6.64(−10) |
| 1.30(−1) | 4.04(−8) | 7.20(−10) |
| 1.38(−1) | 3.88(−8) | 7.17(−10) |
| 1.42(−1) | 3.78(−8) | 6.28(−10) |
| 1.50(−1) | 3.85(−8) | 6.71(−10) |
| 1.54(−1) | 3.66(−8) | 6.54(−10) |
| 1.62(−1) | 3.38(−8) | 6.34(−10) |
| 1.66(−1) | 3.42(−8) | 6.66(−10) |
| 1.74(−1) | 3.14(−8) | 6.01(−10) |
| 1.79(−1) | 3.39(−8) | 7.47(−10) |
| 1.83(−1) | 3.31(−8) | 1.04(−9) |
| 1.87(−1) | 3.58(−8) | 6.10(−10) |
| 1.95(−1) | 3.83(−8) | 5.90(−10) |
| 1.99(−1) | 3.73(−8) | 8.44(−10) |
| 2.03(−1) | 3.81(−8) | 9.11(−10) |
| 2.07(−1) | 3.76(−8) | 5.55(−10) |
| 2.15(−1) | 3.54(−8) | 5.61(−10) |
| 2.24(−1) | 3.84(−8) | 5.78(−10) |
| 2.29(−1) | 4.08(−8) | 6.07(−10) |
| 2.39(−1) | 4.63(−8) | 6.19(−10) |
| 2.44(−1) | 4.56(−8) | 8.53(−10) |
| 2.49(−1) | 4.94(−8) | 1.03(−9) |
| 2.54(−1) | 4.49(−8) | 6.60(−10) |
| 2.59(−1) | 4.29(−8) | 6.96(−10) |
| 2.65(−1) | 4.37(−8) | 1.31(−9) |
| 2.71(−1) | 4.14(−8) | 5.81(−10) |
| 2.76(−1) | 4.39(−8) | 7.29(−10) |
| 2.89(−1) | 4.50(−8) | 6.31(−10) |
| 2.95(−1) | 5.08(−8) | 6.64(−10) |
| 3.01(−1) | 5.36(−8) | 7.23(−10) |
| 3.15(−1) | 5.20(−8) | 7.63(−10) |
| 3.22(−1) | 4.75(−8) | 6.70(−10) |
| 3.30(−1) | 4.45(−8) | 6.44(−10) |
| 3.37(−1) | 3.85(−8) | 6.34(−10) |
| 3.45(−1) | 3.55(−8) | 5.82(−10) |
| 3.61(−1) | 3.27(−8) | 6.30(−10) |
| 3.70(−1) | 3.03(−8) | 5.45(−10) |
| 3.79(−1) | 2.47(−8) | 4.83(−10) |
| 3.88(−1) | 2.13(−8) | 5.40(−10) |
| 3.97(−1) | 1.89(−8) | 4.82(−10) |
| 4.07(−1) | 1.72(−8) | 4.92(−10) |
| 4.17(−1) | 1.52(−8) | 4.88(−10) |
| 4.28(−1) | 1.58(−8) | 5.15(−10) |
| 4.39(−1) | 1.71(−8) | 4.78(−10) |
| 4.50(−1) | 1.98(−8) | 4.89(−10) |
| 4.61(−1) | 2.21(−8) | 5.24(−10) |
| 4.73(−1) | 2.33(−8) | 3.95(−10) |
| 4.86(−1) | 2.55(−8) | 4.97(−10) |
| 4.99(−1) | 2.64(−8) | 5.55(−10) |
| 5.12(−1) | 3.15(−8) | 5.44(−10) |
| 5.26(−1) | 3.27(−8) | 5.93(−10) |
| 5.40(−1) | 2.81(−8) | 4.07(−10) |

**Table 2**
(Continued)

| $E_d$ (eV) | $\alpha_{mb}$ ($cm^3\ s^{-1}$) | Statistical Error ($cm^3\ s^{-1}$) |
|---|---|---|
| 5.56(−1) | 2.42(−8) | 3.89(−10) |
| 5.71(−1) | 2.16(−8) | 5.42(−10) |
| 5.88(−1) | 1.62(−8) | 2.79(−10) |
| 6.05(−1) | 1.44(−8) | 3.64(−10) |
| 6.22(−1) | 1.65(−8) | 3.05(−10) |
| 6.41(−1) | 1.96(−8) | 3.17(−10) |
| 6.60(−1) | 2.33(−8) | 4.19(−10) |
| 6.80(−1) | 2.36(−8) | 3.40(−10) |
| 7.01(−1) | 2.07(−8) | 3.13(−10) |
| 7.24(−1) | 1.62(−8) | 3.71(−10) |
| 7.47(−1) | 1.74(−8) | 2.89(−10) |
| 7.71(−1) | 1.86(−8) | 2.84(−10) |
| 7.97(−1) | 1.81(−8) | 3.26(−10) |
| 8.24(−1) | 1.98(−8) | 3.71(−10) |
| 8.52(−1) | 2.04(−8) | 2.61(−10) |
| 8.82(−1) | 2.01(−8) | 2.47(−10) |
| 9.13(−1) | 1.75(−8) | 2.53(−10) |
| 9.47(−1) | 1.45(−8) | 2.44(−10) |
| 9.82(−1) | 1.24(−8) | 3.22(−10) |
| 1.02(+0) | 1.23(−8) | 5.83(−10) |
| 1.06(+0) | 9.97(−9) | 5.37(−10) |
| 1.10(+0) | 9.40(−9) | 5.13(−10) |
| 1.15(+0) | 9.01(−9) | 5.26(−10) |
| 1.19(+0) | 6.61(−9) | 5.12(−10) |
| 1.25(+0) | 6.38(−9) | 4.75(−10) |
| 1.30(+0) | 6.60(−9) | 3.42(−10) |
| 1.36(+0) | 4.81(−9) | 4.26(−10) |
| 1.42(+0) | 5.58(−9) | 3.34(−10) |
| 1.49(+0) | 3.87(−9) | 4.46(−10) |
| 1.57(+0) | 4.46(−9) | 3.10(−10) |
| 1.64(+0) | 3.86(−9) | 4.27(−10) |
| 1.73(+0) | 3.37(−9) | 2.77(−10) |
| 1.81(+0) | 3.08(−9) | 2.81(−10) |
| 1.90(+0) | 2.94(−9) | 2.76(−10) |
| 1.99(+0) | 3.90(−9) | 4.20(−10) |
| 2.09(+0) | 2.80(−9) | 2.73(−10) |
| 2.19(+0) | 2.91(−9) | 2.95(−10) |
| 2.30(+0) | 2.86(−9) | 2.86(−10) |
| 2.41(+0) | 2.59(−9) | 2.80(−10) |
| 2.53(+0) | 3.46(−9) | 2.98(−10) |
| 2.65(+0) | 3.27(−9) | 3.16(−10) |
| 2.78(+0) | 2.78(−9) | 3.10(−10) |
| 2.91(+0) | 1.61(−9) | 2.12(−10) |
| 3.05(+0) | 1.10(−9) | 2.79(−10) |
| 3.19(+0) | 5.85(−10) | 2.60(−10) |
| 3.34(+0) | 5.23(−10) | 2.81(−10) |
| 3.50(+0) | 5.74(−10) | 2.16(−10) |
| 3.66(+0) | 1.06(−9) | 2.95(−10) |
| 3.83(+0) | 5.28(−10) | 2.17(−10) |
| 4.00(+0) | 7.56(−10) | 2.77(−10) |
| 4.19(+0) | 1.12(−9) | 2.30(−10) |
| 4.38(+0) | 1.16(−9) | 2.86(−10) |
| 4.57(+0) | 1.33(−9) | 2.36(−10) |
| 4.77(+0) | 2.09(−9) | 3.03(−10) |
| 4.98(+0) | 1.65(−9) | 2.37(−10) |
| 5.20(+0) | 1.94(−9) | 2.53(−10) |
| 5.43(+0) | 2.38(−9) | 1.81(−10) |
| 5.66(+0) | 2.37(−9) | 2.35(−10) |
| 5.90(+0) | 2.94(−9) | 1.97(−10) |
| 6.15(+0) | 2.91(−9) | 1.96(−10) |
| 6.40(+0) | 3.85(−9) | 2.25(−10) |
| 6.67(+0) | 3.91(−9) | 3.22(−10) |
| 6.94(+0) | 4.16(−9) | 3.56(−10) |
| 7.22(+0) | 4.50(−9) | 3.65(−10) |
| 7.51(+0) | 4.09(−9) | 3.68(−10) |

**Table 2**
(Continued)

| $E_d$ (eV) | $\alpha_{mb}$ ($cm^3\ s^{-1}$) | Statistical Error ($cm^3\ s^{-1}$) |
|---|---|---|
| 7.81(+0) | 4.31(−9) | 3.10(−10) |
| 8.13(+0) | 5.63(−9) | 3.74(−10) |
| 8.46(+0) | 5.32(−9) | 4.01(−10) |
| 8.81(+0) | 6.61(−9) | 3.79(−10) |
| 9.18(+0) | 7.66(−9) | 3.81(−10) |
| 9.56(+0) | 6.94(−9) | 4.24(−10) |
| 9.97(+0) | 8.10(−9) | 4.21(−10) |
| 1.04(+1) | 7.00(−9) | 3.69(−10) |
| 1.08(+1) | 7.15(−9) | 3.24(−10) |
| 1.13(+1) | 6.73(−9) | 3.88(−10) |
| 1.18(+1) | 6.20(−9) | 3.48(−10) |

**Notes.** The format $x(y)$ signifies $x \times 10^y$. There is an additional systematic uncertainty of 8.4% in the merged-beams rate coefficient (see the text).

of the first energy bin is set to $E = 0$ and is not displayed on the logarithmic energy scale of the plot.

For the conversion of $\alpha_{mb}$ to $\sigma$, we followed the procedure developed by Novotný et al. (2013). The method involves fitting $\alpha_{mb}$ with a model rate coefficient. The fitting yielded a minimum chi-squared of $\chi^2/N_{DF} = 1.49$, where $N_{DF} = 46$ is the number of degrees of freedom in the fit. The conversion procedure allows for propagating the uncertainties of $\alpha_{mb}$ to the cross section. The systematic errors from the absolute scaling, the background subtraction, and the correction on the geometrical detector efficiency propagate all nearly directly, i.e., relative errors in $\sigma$ at $E$ are close to those in $\alpha_{mb}$ at $E_d = E$. The statistical errors also propagate similarly, except for energies $E_d \lesssim k_B T_\parallel^T$, where the statistical uncertainty increases up to 30%.

The uncertainties in the electron beam parameters, primarily in $k_B T_\parallel^T$ and $k_B T_\perp^T$, also affect the cross-section error. We calculate this error by modeling the experimental electron-ion collision energy distribution. The corresponding uncertainties in $\sigma$ are displayed as gray bars in Figure 3. The largest sensitivity can be seen at collision energies $E_d \lesssim k_B T_\parallel^T$, where the collision energy spread is comparable to the mean collision energy. Some enhanced uncertainties appear also at $E \approx 0.1$ eV. This is due to the cross-section bins being comparable in width to the energy spread at these energies.

### 4.3. Plasma Recombination Rate Coefficient

We have converted $\sigma$ to a plasma rate coefficient using the procedures described in Section 3.4. The resulting $\alpha_{pl}(T_{pl})$ is plotted in Figure 4 for a plasma temperature range of $T_{pl}$ = 10–18,000 K. Note that $T_{pl}$ represents only the spread in the collision energies between the electrons and ions. As discussed in Section 3.2, the internal excitation of the studied ions is expected to be ∼300 K.

The statistical uncertainties propagate to $\alpha_{pl}$ at very low levels, amounting to less than 1% at all temperatures. This is due to the integrative nature of the transformation from $\sigma$ to $\alpha_{pl}$. Three systematic errors are relevant in the given temperature range for the plasma rate coefficient. First, the absolute scaling error of $\alpha_{mb}$ propagates directly to $\alpha_{pl}$ as an 8.4% relative error, which describes a single scaling of the complete $\alpha_{pl}(T_{pl})$ curve. Second, the background subtraction uncertainty generates an absolute error in $\alpha_{pl}$ of $\pm 7 \times 10^{-10}$ $cm^3\ s^{-1}$, independent of $T_{pl}$. Lastly, the uncertainties of the electron beam parameters

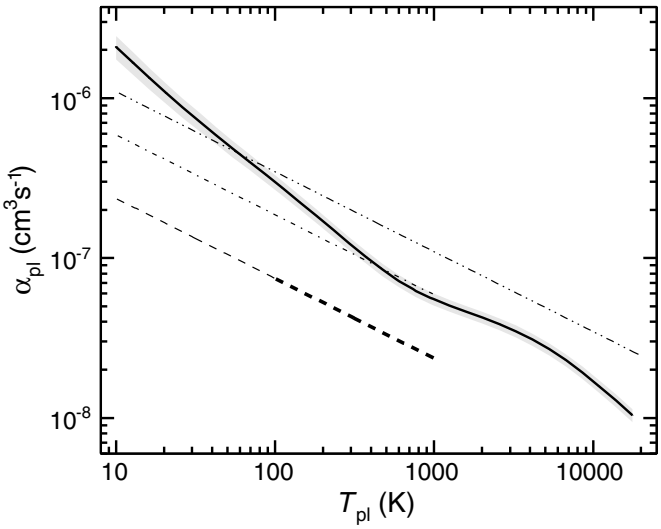


**Figure 4.** Experimentally derived DR plasma rate coefficient for $NH^+$ plotted vs. the collisional plasma temperature (full black line). The gray band marks the total systematic uncertainty originating from the error on the absolute scaling, background subtraction, detector geometrical efficiency correction, and uncertainties in $k_B T_\perp^T$ and $k_B T_\parallel^T$. The statistical errors propagated from $\alpha_{mb}$ are smaller than 1% at all temperatures and thus indistinguishable in the plot. The thick dashed line plots the previous DR $NH^+$ results of McGowan et al. (1979), corrected for an erroneous form factor (Mitchell 1990; J. B. A. Mitchell 2012, private communication), in the approximate temperature range of validity. The thin dashed line extrapolates these data down to $T_{pl}$ = 10 K as it is done in current astrochemical models. The thin dot-dashed line plots the same curve but without the correction for the erroneous form factor. These uncorrected data are used in some of the astrochemical databases. The dot-dot-dashed line plots $\alpha_{pl}^{di}$, which represents a "typical" rate coefficient for diatomic ions.

propagate to $\alpha_{pl}$ as an absolute error, which can be well approximated by $\pm 6.1 \times 10^{-6}\ (T_{pl}/K)^{-1.3}\ cm^3\ s^{-1}$. The behavior of the various systematic errors needs to be taken into account when propagating the resulting rate coefficient uncertainties. For chemical models involving a range of temperatures, the three systematic errors must be applied to all $\alpha_{pl}(T_{pl})$ points in a correlated way according to the description given. For models at a single fixed temperature, their appropriate absolute values can be added in quadrature. This results in a systematic error of ∼16% at $T_{pl}$ = 10 K, ∼10% at 100 K, ∼8% at 1000 K, ∼9% at 10,000 K, and ∼9% at 18,000 K.

To parameterize the results for use in astrochemical modeling, we have fit the data with an analytical formula. We tried to fit the data with both the two- and three-parameter functions commonly used to describe DR plasma rate coefficients in astrochemical models and databases (e.g., Florescu-Mitchell & Mitchell 2006; Wakelam 2010), but were unable to fit our measured plasma rate coefficient over the entire temperature range with a precision of any better than 40%. Therefore, we used the form proposed by Novotný et al. (2013), namely

$$\alpha_{pl}^{fit}(T_{pl}) = A \left(\frac{300\ K}{T_{pl}}\right)^n + B, \quad (6)$$

where

$$B = T_{pl}^{-3/2} \sum_{i=1}^{4} c_i \exp(-T_i/T_{pl}). \quad (7)$$

We fit Equation (6) to our data over the full temperature range. The resulting parameters are given in Table 4. The deviations of $\alpha_{pl}^{fit}$ from the data are less than 1% over the reported temperature range.

**Table 3**
Cross Section $\sigma$ for DR of $NH^+$

| $E_{center}$ (eV) | $E_{width}$ (eV) | $\sigma$ ($cm^2$) | $U^{lo}_{stat}$ ($cm^2$) | $U^{hi}_{stat}$ ($cm^2$) | $U^{lo}_{syst}$ ($cm^2$) | $U^{hi}_{syst}$ ($cm^2$) |
|---|---|---|---|---|---|---|
| 1.65(−5) | 3.30(−5) | 1.28(−10) | −4.38(−11) | +4.16(−11) | −2.76(−11) | +2.15(−10) |
| 8.36(−5) | 1.01(−4) | 3.86(−11) | −5.16(−12) | +5.58(−12) | −7.80(−12) | +8.19(−12) |
| 2.52(−4) | 2.35(−4) | 4.43(−12) | −6.96(−13) | +6.58(−13) | −1.77(−12) | +6.87(−13) |
| 6.13(−4) | 4.88(−4) | 7.86(−13) | −9.02(−14) | +9.17(−14) | −1.37(−13) | +1.13(−13) |
| 1.35(−3) | 9.87(−4) | 3.12(−13) | −1.89(−14) | +1.77(−14) | −3.09(−14) | +3.14(−14) |
| 2.52(−3) | 1.35(−3) | 1.67(−13) | −6.70(−15) | +6.79(−15) | −1.64(−14) | +1.63(−14) |
| 3.93(−3) | 1.48(−3) | 9.62(−14) | −3.31(−15) | +2.88(−15) | −1.02(−14) | +8.32(−15) |
| 5.48(−3) | 1.61(−3) | 7.45(−14) | −1.88(−15) | +1.90(−15) | −6.90(−15) | +8.27(−15) |
| 7.16(−3) | 1.75(−3) | 4.95(−14) | −1.26(−15) | +1.31(−15) | −5.36(−15) | +4.45(−15) |
| 8.97(−3) | 1.88(−3) | 3.69(−14) | −1.21(−15) | +1.03(−15) | −3.26(−15) | +3.77(−15) |
| 1.09(−2) | 2.01(−3) | 2.72(−14) | −9.67(−16) | +9.75(−16) | −2.92(−15) | +2.33(−15) |
| 1.30(−2) | 2.15(−3) | 2.26(−14) | −7.54(−16) | +8.89(−16) | −1.93(−15) | +2.08(−15) |
| 1.52(−2) | 2.28(−3) | 1.92(−14) | −7.69(−16) | +6.85(−16) | −1.70(−15) | +1.66(−15) |
| 1.76(−2) | 2.42(−3) | 1.65(−14) | −6.76(−16) | +6.70(−16) | −1.44(−15) | +1.55(−15) |
| 2.01(−2) | 2.55(−3) | 1.25(−14) | −5.19(−16) | +5.21(−16) | −1.19(−15) | +1.09(−15) |
| 2.27(−2) | 2.69(−3) | 1.10(−14) | −4.55(−16) | +5.13(−16) | −9.54(−16) | +9.63(−16) |
| 2.54(−2) | 2.82(−3) | 9.35(−15) | −4.00(−16) | +4.28(−16) | −8.38(−16) | +9.29(−16) |
| 2.83(−2) | 2.96(−3) | 7.35(−15) | −4.21(−16) | +3.27(−16) | −9.52(−16) | +6.48(−16) |
| 3.13(−2) | 3.09(−3) | 6.92(−15) | −4.04(−16) | +4.53(−16) | −6.32(−16) | +9.05(−16) |
| 3.45(−2) | 3.23(−3) | 5.45(−15) | −3.72(−16) | +4.13(−16) | −6.10(−16) | +5.21(−16) |
| 3.78(−2) | 3.36(−3) | 4.43(−15) | −3.42(−16) | +3.00(−16) | −4.35(−16) | +4.55(−16) |
| 4.12(−2) | 3.50(−3) | 3.65(−15) | −1.68(−16) | +1.62(−16) | −5.36(−16) | +3.48(−16) |
| 4.48(−2) | 3.64(−3) | 3.71(−15) | −1.57(−16) | +1.32(−16) | −3.65(−16) | +6.00(−16) |
| 4.85(−2) | 3.77(−3) | 2.70(−15) | −1.26(−16) | +1.35(−16) | −4.08(−16) | +2.73(−16) |
| 5.24(−2) | 3.91(−3) | 2.23(−15) | −1.28(−16) | +1.13(−16) | −2.36(−16) | +2.74(−16) |
| 5.63(−2) | 4.05(−3) | 1.82(−15) | −9.06(−17) | +9.43(−17) | −2.21(−16) | +1.98(−16) |
| 6.04(−2) | 4.18(−3) | 1.65(−15) | −8.59(−17) | +8.45(−17) | −1.84(−16) | +1.82(−16) |
| 6.47(−2) | 4.32(−3) | 1.64(−15) | −1.08(−16) | +8.91(−17) | −1.84(−16) | +2.06(−16) |
| 6.91(−2) | 4.45(−3) | 1.40(−15) | −1.06(−16) | +1.15(−16) | −2.46(−16) | +1.56(−16) |
| 7.36(−2) | 4.59(−3) | 1.71(−15) | −1.09(−16) | +1.10(−16) | −1.84(−16) | +2.81(−16) |
| 7.83(−2) | 4.73(−3) | 1.57(−15) | −1.68(−16) | +1.74(−16) | −2.40(−16) | +1.72(−16) |
| 8.31(−2) | 4.86(−3) | 1.78(−15) | −1.41(−16) | +1.30(−16) | −1.88(−16) | +2.62(−16) |
| 8.80(−2) | 5.00(−3) | 1.64(−15) | −1.07(−16) | +1.21(−16) | −2.80(−16) | +1.72(−16) |
| 9.31(−2) | 5.14(−3) | 1.80(−15) | −1.62(−16) | +1.38(−16) | −1.85(−16) | +3.15(−16) |
| 9.83(−2) | 5.27(−3) | 1.65(−15) | −8.93(−17) | +9.83(−17) | −3.37(−16) | +1.70(−16) |
| 1.04(−1) | 5.41(−3) | 1.91(−15) | −1.28(−16) | +1.22(−16) | −1.95(−16) | +3.56(−16) |
| 1.09(−1) | 5.55(−3) | 1.63(−15) | −7.99(−17) | +7.66(−17) | −3.02(−16) | +1.65(−16) |
| 1.15(−1) | 5.69(−3) | 1.90(−15) | −1.04(−16) | +9.87(−17) | −1.83(−16) | +2.02(−16) |
| 1.20(−1) | 5.82(−3) | 2.18(−15) | −7.33(−17) | +8.23(−17) | −2.06(−16) | +2.06(−16) |
| 1.26(−1) | 5.96(−3) | 2.21(−15) | −9.81(−17) | +8.17(−17) | −2.09(−16) | +2.61(−16) |
| 1.32(−1) | 6.10(−3) | 1.98(−15) | −7.74(−17) | +8.00(−17) | −2.56(−16) | +1.91(−16) |
| 1.39(−1) | 6.23(−3) | 1.92(−15) | −7.52(−17) | +8.76(−17) | −1.84(−16) | +3.06(−16) |
| 1.45(−1) | 6.37(−3) | 1.73(−15) | −8.21(−17) | +7.22(−17) | −3.74(−16) | +1.67(−16) |
| 1.51(−1) | 6.51(−3) | 1.88(−15) | −7.06(−17) | +7.73(−17) | −1.82(−16) | +4.51(−16) |
| 1.58(−1) | 6.64(−3) | 1.53(−15) | −8.57(−17) | +8.73(−17) | −4.03(−16) | +1.52(−16) |
| 1.65(−1) | 6.78(−3) | 1.52(−15) | −6.82(−17) | +6.45(−17) | −1.51(−16) | +3.14(−16) |
| 1.71(−1) | 6.92(−3) | 1.35(−15) | −1.07(−16) | +9.58(−17) | −2.62(−16) | +1.36(−16) |
| 1.78(−1) | 7.06(−3) | 1.32(−15) | −6.06(−17) | +6.17(−17) | −1.32(−16) | +1.73(−16) |
| 1.86(−1) | 7.19(−3) | 1.36(−15) | −6.86(−17) | +7.40(−17) | −1.87(−16) | +1.34(−16) |
| 1.93(−1) | 7.33(−3) | 1.62(−15) | −9.83(−17) | +8.85(−17) | −1.57(−16) | +2.00(−16) |
| 2.00(−1) | 7.47(−3) | 1.48(−15) | −6.17(−17) | +7.17(−17) | −1.74(−16) | +1.43(−16) |
| 2.08(−1) | 7.61(−3) | 1.53(−15) | −4.42(−17) | +4.28(−17) | −1.48(−16) | +1.86(−16) |
| 2.15(−1) | 7.74(−3) | 1.30(−15) | −4.92(−17) | +5.15(−17) | −1.46(−16) | +1.27(−16) |
| 2.23(−1) | 7.88(−3) | 1.37(−15) | −5.99(−17) | +6.45(−17) | −1.47(−16) | +1.32(−16) |
| 2.31(−1) | 8.02(−3) | 1.53(−15) | −5.01(−17) | +4.76(−17) | −1.44(−16) | +1.55(−16) |
| 2.39(−1) | 8.16(−3) | 1.72(−15) | −5.16(−17) | +4.74(−17) | −1.64(−16) | +1.59(−16) |
| 2.47(−1) | 8.29(−3) | 1.80(−15) | −5.25(−17) | +6.46(−17) | −1.65(−16) | +1.86(−16) |
| 2.56(−1) | 8.43(−3) | 1.64(−15) | −5.00(−17) | +4.78(−17) | −1.53(−16) | +1.53(−16) |
| 2.64(−1) | 8.57(−3) | 1.50(−15) | −5.37(−17) | +6.41(−17) | −1.43(−16) | +1.41(−16) |
| 2.73(−1) | 8.71(−3) | 1.40(−15) | −4.23(−17) | +4.74(−17) | −1.40(−16) | +1.32(−16) |
| 2.82(−1) | 8.84(−3) | 1.62(−15) | −7.37(−17) | +6.95(−17) | −1.51(−16) | +1.73(−16) |
| 2.91(−1) | 8.98(−3) | 1.46(−15) | −3.97(−17) | +4.09(−17) | −2.29(−16) | +1.36(−16) |
| 3.00(−1) | 9.12(−3) | 1.89(−15) | −4.32(−17) | +4.50(−17) | −1.71(−16) | +2.16(−16) |
| 3.11(−1) | 1.44(−2) | 1.86(−15) | −5.21(−17) | +5.21(−17) | −1.69(−16) | +1.71(−16) |
| 3.22(−1) | 7.25(−3) | 1.57(−15) | −5.91(−17) | +6.68(−17) | −1.64(−16) | +1.47(−16) |

**Table 3**
(Continued)

| $E_{\rm center}$ (eV) | $E_{\rm width}$ (eV) | $\sigma$ (cm$^2$) | $U_{\rm stat}^{\rm lo}$ (cm$^2$) | $U_{\rm stat}^{\rm hi}$ (cm$^2$) | $U_{\rm syst}^{\rm lo}$ (cm$^2$) | $U_{\rm syst}^{\rm hi}$ (cm$^2$) |
|---|---|---|---|---|---|---|
| 3.30(−1) | 7.47(−3) | 1.58(−15) | −6.43(−17) | +5.95(−17) | −1.51(−16) | +1.99(−16) |
| 3.37(−1) | 7.70(−3) | 1.26(−15) | −5.21(−17) | +5.77(−17) | −1.59(−16) | +1.23(−16) |
| 3.47(−1) | 1.21(−2) | 1.12(−15) | −3.15(−17) | +2.61(−17) | −1.10(−16) | +1.12(−16) |
| 3.59(−1) | 1.25(−2) | 1.03(−15) | −3.69(−17) | +4.18(−17) | −1.25(−16) | +1.02(−16) |
| 3.70(−1) | 8.71(−3) | 1.01(−15) | −3.98(−17) | +3.71(−17) | −1.02(−16) | +2.05(−16) |
| 3.79(−1) | 9.00(−3) | 7.46(−16) | −3.44(−17) | +3.23(−17) | −1.67(−16) | +8.03(−17) |
| 3.88(−1) | 9.29(−3) | 6.29(−16) | −3.33(−17) | +3.55(−17) | −7.22(−17) | +1.04(−16) |
| 3.97(−1) | 9.60(−3) | 5.31(−16) | −2.94(−17) | +2.98(−17) | −9.56(−17) | +6.39(−17) |
| 4.07(−1) | 9.92(−3) | 4.92(−16) | −3.00(−17) | +3.05(−17) | −6.35(−17) | +9.55(−17) |
| 4.17(−1) | 1.03(−2) | 3.75(−16) | −2.69(−17) | +2.84(−17) | −8.89(−17) | +5.08(−17) |
| 4.28(−1) | 1.06(−2) | 3.98(−16) | −2.80(−17) | +2.77(−17) | −5.19(−17) | +5.81(−17) |
| 4.39(−1) | 1.10(−2) | 4.14(−16) | −2.61(−17) | +2.50(−17) | −5.63(−17) | +5.32(−17) |
| 4.50(−1) | 1.14(−2) | 4.96(−16) | −2.49(−17) | +2.29(−17) | −6.13(−17) | +5.87(−17) |
| 4.61(−1) | 1.18(−2) | 5.75(−16) | −2.43(−17) | +2.40(−17) | −6.45(−17) | +8.27(−17) |
| 4.73(−1) | 1.22(−2) | 5.80(−16) | −1.96(−17) | +1.96(−17) | −8.99(−17) | +6.52(−17) |
| 4.86(−1) | 1.27(−2) | 6.68(−16) | −2.21(−17) | +2.14(−17) | −7.03(−17) | +9.85(−17) |
| 4.99(−1) | 1.32(−2) | 6.39(−16) | −2.36(−17) | +2.31(−17) | −1.01(−16) | +6.57(−17) |
| 5.12(−1) | 1.37(−2) | 8.15(−16) | −2.14(−17) | +2.25(−17) | −8.12(−17) | +8.48(−17) |
| 5.26(−1) | 1.42(−2) | 8.81(−16) | −2.38(−17) | +2.32(−17) | −8.77(−17) | +9.41(−17) |
| 5.41(−1) | 1.48(−2) | 7.26(−16) | −1.56(−17) | +1.55(−17) | −7.58(−17) | +7.62(−17) |
| 5.56(−1) | 1.54(−2) | 6.03(−16) | −1.58(−17) | +1.38(−17) | −7.16(−17) | +6.46(−17) |
| 5.71(−1) | 1.60(−2) | 5.49(−16) | −1.68(−17) | +1.82(−17) | −6.24(−17) | +7.36(−17) |
| 5.88(−1) | 1.67(−2) | 3.74(−16) | −1.04(−17) | +9.33(−18) | −5.15(−17) | +4.90(−17) |
| 6.05(−1) | 1.74(−2) | 3.05(−16) | −1.13(−17) | +1.18(−17) | −4.77(−17) | +4.43(−17) |
| 6.22(−1) | 1.81(−2) | 3.55(−16) | −9.79(−18) | +8.36(−18) | −4.62(−17) | +4.62(−17) |
| 6.41(−1) | 1.89(−2) | 4.26(−16) | −9.19(−18) | +1.00(−17) | −5.10(−17) | +4.96(−17) |
| 6.60(−1) | 1.98(−2) | 5.28(−16) | −1.38(−17) | +1.18(−17) | −5.71(−17) | +5.79(−17) |
| 6.81(−1) | 2.07(−2) | 5.38(−16) | −9.75(−18) | +9.36(−18) | −5.88(−17) | +5.92(−17) |
| 7.02(−1) | 2.16(−2) | 4.65(−16) | −9.49(−18) | +8.22(−18) | −5.33(−17) | +5.58(−17) |
| 7.24(−1) | 2.27(−2) | 3.32(−16) | −1.03(−17) | +1.04(−17) | −4.79(−17) | +4.35(−17) |
| 7.47(−1) | 2.38(−2) | 3.59(−16) | −7.03(−18) | +7.90(−18) | −4.58(−17) | +4.58(−17) |
| 7.71(−1) | 2.50(−2) | 3.85(−16) | −7.09(−18) | +7.62(−18) | −4.69(−17) | +4.72(−17) |
| 7.97(−1) | 2.63(−2) | 3.63(−16) | −8.34(−18) | +8.15(−18) | −4.63(−17) | +4.58(−17) |
| 8.24(−1) | 2.76(−2) | 4.01(−16) | −7.89(−18) | +8.58(−18) | −4.63(−17) | +4.63(−17) |
| 8.52(−1) | 2.91(−2) | 4.10(−16) | −5.70(−18) | +6.40(−18) | −4.81(−17) | +4.81(−17) |
| 8.82(−1) | 3.07(−2) | 4.03(−16) | −5.69(−18) | +5.82(−18) | −4.79(−17) | +4.82(−17) |
| 9.14(−1) | 3.24(−2) | 3.45(−16) | −5.53(−18) | +5.69(−18) | −4.31(−17) | +4.32(−17) |
| 9.47(−1) | 3.43(−2) | 2.77(−16) | −5.18(−18) | +5.31(−18) | −3.95(−17) | +3.95(−17) |
| 9.83(−1) | 3.63(−2) | 2.29(−16) | −6.65(−18) | +6.83(−18) | −3.72(−17) | +3.70(−17) |
| 1.02(+0) | 3.85(−2) | 2.26(−16) | −1.15(−17) | +1.33(−17) | −2.16(−17) | +2.23(−17) |
| 1.06(+0) | 4.09(−2) | 1.77(−16) | −9.88(−18) | +1.01(−17) | −1.74(−17) | +1.74(−17) |
| 1.10(+0) | 4.36(−2) | 1.64(−16) | −1.06(−17) | +9.14(−18) | −1.62(−17) | +1.62(−17) |
| 1.15(+0) | 4.64(−2) | 1.56(−16) | −1.09(−17) | +1.03(−17) | −1.56(−17) | +1.57(−17) |
| 1.19(+0) | 4.96(−2) | 1.09(−16) | −1.02(−17) | +9.20(−18) | −1.15(−17) | +1.15(−17) |
| 1.25(+0) | 5.31(−2) | 1.03(−16) | −9.35(−18) | +8.48(−18) | −1.09(−17) | +1.09(−17) |
| 1.30(+0) | 5.70(−2) | 1.06(−16) | −6.24(−18) | +6.42(−18) | −1.13(−17) | +1.15(−17) |
| 1.36(+0) | 6.13(−2) | 7.27(−17) | −7.63(−18) | +6.92(−18) | −8.43(−18) | +8.40(−18) |
| 1.42(+0) | 6.61(−2) | 8.52(−17) | −5.89(−18) | +5.11(−18) | −9.50(−18) | +9.45(−18) |
| 1.49(+0) | 7.12(−2) | 5.52(−17) | −7.17(−18) | +7.35(−18) | −6.92(−18) | +6.93(−18) |
| 1.57(+0) | 7.59(−2) | 6.39(−17) | −4.96(−18) | +5.08(−18) | −7.61(−18) | +7.62(−18) |
| 1.64(+0) | 7.99(−2) | 5.35(−17) | −6.73(−18) | +6.77(−18) | −6.75(−18) | +6.78(−18) |
| 1.73(+0) | 8.36(−2) | 4.50(−17) | −4.13(−18) | +4.14(−18) | −6.05(−18) | +6.06(−18) |
| 1.81(+0) | 8.75(−2) | 3.97(−17) | −4.34(−18) | +4.14(−18) | −5.68(−18) | +5.66(−18) |
| 1.90(+0) | 9.16(−2) | 3.66(−17) | −3.80(−18) | +4.03(−18) | −5.24(−18) | +5.25(−18) |
| 2.00(+0) | 9.58(−2) | 4.98(−17) | −5.83(−18) | +5.97(−18) | −6.40(−18) | +6.43(−18) |
| 2.09(+0) | 1.00(−1) | 3.36(−17) | −3.95(−18) | +3.63(−18) | −4.96(−18) | +4.96(−18) |
| 2.20(+0) | 1.05(−1) | 3.45(−17) | −3.79(−18) | +4.12(−18) | −4.98(−18) | +4.98(−18) |
| 2.30(+0) | 1.09(−1) | 3.32(−17) | −4.13(−18) | +3.58(−18) | −4.86(−18) | +4.85(−18) |
| 2.41(+0) | 1.14(−1) | 2.87(−17) | −3.42(−18) | +3.34(−18) | −4.45(−18) | +4.45(−18) |
| 2.53(+0) | 1.19(−1) | 3.93(−17) | −3.74(−18) | +3.71(−18) | −5.23(−18) | +5.23(−18) |
| 2.65(+0) | 1.24(−1) | 3.66(−17) | −3.91(−18) | +4.07(−18) | −5.01(−18) | +5.02(−18) |
| 2.78(+0) | 1.30(−1) | 3.06(−17) | −4.08(−18) | +3.55(−18) | −4.60(−18) | +4.59(−18) |
| 2.91(+0) | 1.35(−1) | 1.68(−17) | −2.59(−18) | +2.26(−18) | −3.62(−18) | +3.61(−18) |
| 3.05(+0) | 1.41(−1) | 1.09(−17) | −3.02(−18) | +3.28(−18) | −3.42(−18) | +3.44(−18) |
| 3.19(+0) | 1.47(−1) | 4.94(−18) | −2.52(−18) | +2.99(−18) | −2.75(−18) | +2.81(−18) |

**Table 3**
(Continued)

| $E_{center}$ (eV) | $E_{width}$ (eV) | $\sigma$ (cm$^2$) | $U_{stat}^{lo}$ (cm$^2$) | $U_{stat}^{hi}$ (cm$^2$) | $U_{syst}^{lo}$ (cm$^2$) | $U_{syst}^{hi}$ (cm$^2$) |
|---|---|---|---|---|---|---|
| 3.34(+0) | 1.53(−1) | 4.00(−18) | −2.58(−18) | +3.09(−18) | −2.49(−18) | +2.49(−18) |
| 3.50(+0) | 1.59(−1) | 4.18(−18) | −2.06(−18) | +2.37(−18) | −2.36(−18) | +2.37(−18) |
| 3.66(+0) | 1.65(−1) | 9.06(−18) | −2.80(−18) | +2.95(−18) | −3.04(−18) | +3.05(−18) |
| 3.83(+0) | 1.72(−1) | 3.31(−18) | −1.81(−18) | +2.36(−18) | −2.03(−18) | +2.10(−18) |
| 4.01(+0) | 1.79(−1) | 5.15(−18) | −2.49(−18) | +2.87(−18) | −2.30(−18) | +2.35(−18) |
| 4.19(+0) | 1.85(−1) | 8.29(−18) | −2.32(−18) | +2.01(−18) | −2.59(−18) | +2.59(−18) |
| 4.38(+0) | 1.92(−1) | 8.17(−18) | −2.42(−18) | +2.59(−18) | −2.49(−18) | +2.49(−18) |
| 4.57(+0) | 1.99(−1) | 9.22(−18) | −2.15(−18) | +2.14(−18) | −2.50(−18) | +2.51(−18) |
| 4.78(+0) | 2.07(−1) | 1.57(−17) | −2.37(−18) | +2.65(−18) | −3.04(−18) | +3.09(−18) |
| 4.99(+0) | 2.14(−1) | 1.13(−17) | −1.88(−18) | +2.11(−18) | −2.59(−18) | +2.62(−18) |
| 5.20(+0) | 2.21(−1) | 1.32(−17) | −2.15(−18) | +1.97(−18) | −2.77(−18) | +2.73(−18) |
| 5.43(+0) | 2.29(−1) | 1.64(−17) | −1.49(−18) | +1.52(−18) | −2.90(−18) | +2.90(−18) |
| 5.66(+0) | 2.36(−1) | 1.56(−17) | −1.90(−18) | +1.96(−18) | −2.77(−18) | +2.77(−18) |
| 5.90(+0) | 2.44(−1) | 1.95(−17) | −1.43(−18) | +1.68(−18) | −3.05(−18) | +3.07(−18) |
| 6.15(+0) | 2.52(−1) | 1.85(−17) | −1.49(−18) | +1.43(−18) | −2.93(−18) | +2.93(−18) |
| 6.40(+0) | 2.59(−1) | 2.50(−17) | −1.53(−18) | +1.69(−18) | −3.41(−18) | +3.42(−18) |
| 6.67(+0) | 2.67(−1) | 2.47(−17) | −2.38(−18) | +2.33(−18) | −3.38(−18) | +3.39(−18) |
| 6.94(+0) | 2.75(−1) | 2.59(−17) | −2.72(−18) | +2.48(−18) | −3.42(−18) | +3.41(−18) |
| 7.22(+0) | 2.85(−1) | 2.76(−17) | −2.66(−18) | +2.34(−18) | −3.54(−18) | +3.53(−18) |
| 7.51(+0) | 2.97(−1) | 2.39(−17) | −2.32(−18) | +2.85(−18) | −3.19(−18) | +3.23(−18) |
| 7.81(+0) | 3.11(−1) | 2.45(−17) | −2.06(−18) | +2.18(−18) | −3.20(−18) | +3.21(−18) |
| 8.13(+0) | 3.26(−1) | 3.27(−17) | −2.54(−18) | +2.38(−18) | −3.86(−18) | +3.84(−18) |
| 8.47(+0) | 3.42(−1) | 2.96(−17) | −2.36(−18) | +2.66(−18) | −3.55(−18) | +3.56(−18) |
| 8.82(+0) | 3.59(−1) | 3.70(−17) | −2.27(−18) | +2.55(−18) | −4.15(−18) | +4.18(−18) |
| 9.18(+0) | 3.76(−1) | 4.29(−17) | −2.34(−18) | +2.20(−18) | −4.63(−18) | +4.63(−18) |
| 9.57(+0) | 3.95(−1) | 3.75(−17) | −2.88(−18) | +2.49(−18) | −4.22(−18) | +4.18(−18) |
| 9.97(+0) | 4.16(−1) | 4.41(−17) | −2.36(−18) | +2.38(−18) | −4.72(−18) | +4.72(−18) |
| 1.04(+1) | 4.37(−1) | 3.71(−17) | −2.04(−18) | +2.33(−18) | −4.13(−18) | +4.14(−18) |
| 1.08(+1) | 4.60(−1) | 3.76(−17) | −2.03(−18) | +1.80(−18) | −4.17(−18) | +4.17(−18) |
| 1.13(+1) | 4.85(−1) | 3.50(−17) | −2.27(−18) | +2.12(−18) | −3.96(−18) | +3.96(−18) |
| 1.18(+1) | 5.11(−1) | 3.18(−17) | −1.80(−18) | +1.77(−18) | −3.71(−18) | +3.71(−18) |
| 1.25(+1) | 8.11(−1) | 3.21(−17) | −1.59(−18) | +1.94(−18) | −3.75(−18) | +3.75(−18) |

**Notes.** The binned cross section is given as a function of bin energy center, $E_{center}$. Also listed is the energy width, $E_{width}$, of each bin. The bin start and end energies can be obtained as $E_{center} \mp 0.5 E_{width}$. The asymmetric statistical and systematic uncertainties are given by $U_{stat}$ and $U_{syst}$, respectively. The superscripts "lo" and "hi" give the lower and upper limits, respectively, for the corresponding uncertainties. The total systematic error in the table includes the 8.4% absolute scaling error and the uncertainties from background correction, detector geometrical efficiency correction, and $k_B T_\perp^T$ and $k_B T_\parallel^T$ (see the text). The format $x(y)$ signifies $x \times 10^y$.

## 5. DISCUSSION

### 5.1. Experimental DR Rate Coefficient and Cross Section

The evolution of the $NH^+$ DR rate coefficient with collision energy displays diverse features, which can be used to probe the underlying quantum nature of the process. For clarity, we use Roman numerals to label the features in Figures 1, 2, and 3, which we discuss below. We also plot the thresholds for the opening of various DR product excitation channels. Additionally, we include in the figures the energies of various $NH^+$ states, which are upper limits for Rydberg series of NH states. As we have discussed in Section 2, these neutral states are potentially involved in both direct and indirect DR processes, and their energies may be reflected in the DR energy spectrum.

The overall shapes of $\alpha_{mb}$ and $\sigma$ are dominated by a decreasing magnitude with increasing energy, roughly following the $\sigma \propto E^{-1}$ expected for direct DR process (Florescu-Mitchell & Mitchell 2006; Larsson & Orel 2008). Numerous structures appear on top of this global shape. Three broad features (labeled I, II, and III) are visible at energies below ∼0.05 eV. The features at these low collision energies can be caused by electron capture to rotationally excited NH Rydberg states converging to the $NH^+$ $X\,^2\Pi_{1/2}$, $X\,^2\Pi_{3/2}$, and $a\,^4\Sigma^-$ ionic cores. The decreasing strength of these features with increasing collision energy can be attributed to the opening up of additional

**Table 4**
Fit Parameters for the $NH^+$ DR Plasma Rate Coefficient $\alpha_{pl}$ using Equation (6)

| Parameter | Value | | Units |
|---|---|---|---|
| | $x$ | $y$ | |
| A | 2.11 | −7 | cm$^3$ s$^{-1}$ |
| $n$ | 7.90 | −1 | dimensionless |
| $c_1$ | −1.12 | −4 | K$^{3/2}$ cm$^3$ s$^{-1}$ |
| $c_2$ | −2.49 | −4 | K$^{3/2}$ cm$^3$ s$^{-1}$ |
| $c_3$ | −9.14 | −4 | K$^{3/2}$ cm$^3$ s$^{-1}$ |
| $c_4$ | 8.05 | −3 | K$^{3/2}$ cm$^3$ s$^{-1}$ |
| $T_1$ | 1.28 | 1 | K |
| $T_2$ | 9.24 | 1 | K |
| $T_3$ | 4.81 | 2 | K |
| $T_4$ | 5.03 | 3 | K |

**Notes.** The value for each parameter is given by $x \times 10^y$.

autoionization channels, though individual resonances cannot be distinguished due to the experimental energy resolution. Similar features, which are associated with an even stronger cross-section decrease for increasing energy, were seen for DR of $HCl^+$ (Novotný et al. 2013) where a detailed discussion of this effect was also given.

We have excluded the possibility that these three low-energy structures are an experimental artifact due to ion beam dragging. The concern is that if the electron beam is detuned slightly from the cooling energy, such as for measurements at low collision energies, then Coulomb forces between the beams can drag the ion beam to match the velocity of the electrons. As a consequence, the real collision energy would differ from that calculated by Equation (5). As discussed in Novotný et al. (2013), this distorts the curve of $\alpha_{\rm mb}$ at low collision energies and may appear as a low energy peak. However, our experimental configuration with two electron beams greatly minimizes this effect by enabling us to simultaneously cool the stored ions with the Cooler while measuring DR data using the Target. Additionally, we have performed a set of tests similar to Novotný et al. (2013) that further excluded ion beam dragging as the origin for these features.

In the collision energy range between ∼0.05 eV and ∼3 eV, a significant enhancement is observed of the DR merged-beams rate coefficient compared to the $E^{-1}$ dependence for direct DR, as can be seen in Figure 3. The rather narrow substructures in this energy range (IV to XII, best seen in Figure 2) suggest that indirect DR is contributing in this energy range. Possible origins for the structure seen include DR pathways via NH states with electronically excited ion cores, DR pathways via NH states with vibrationally excited ion cores, and the opening of new final channels as we now describe.

At these energies, similarly strong enhancements were seen for $OH^+$ (Amitay et al. 1996b). There the comparison with calculated data indicated that the enhancements stemmed from indirect DR through neutral Rydberg resonances associated with bound, electronically excited ion-core molecular states. Comparable DR enhancements, possibly of the same origin, have also been observed for $CD^+$ (Forck et al. 1994), $N_2^+$ (Peterson et al. 1998), and several other systems (Amitay et al. 1996a; Tanabe et al. 1998; Padellec et al. 1999; Novotný et al. 2009). For $NH^+$ neutral resonances of this type are expected to occur below the three bound excited states $A\,^2\Sigma^-$, $B\,^2\Delta$, and $C\,^2\Sigma^+$, i.e., in the energy range of where the observed structure indeed occurs in the measured DR rate coefficient. However, we are unaware of any published potential energy curves for doubly excited bound neutral NH. Lacking such calculations, the observed structures cannot be uniquely assigned to specific DR pathways via the neutral Rydberg series converging to the ionic A, B, or C states. Nevertheless, as explained in Section 2, a noticeable change in the DR rate is expected when scanning over a Rydberg series limit converging to an ionic state. In the $NH^+$ DR spectrum, such a threshold feature can be identified for the $v = 0$ level of the A and B ionic states at ∼2.7 eV as a drop in the DR rate coefficient (structure XII). Interestingly, no clear feature in $\alpha_{\rm mb}$ can be found at the excitation energy of the $C\,^2\Sigma^+$ state of $NH^+$.

In addition to the above DR via neutral Rydberg states converging to excited electronic ionic states, some of the sub-structures in $\alpha_{\rm mb}$ above ∼0.05 eV may also be due to electron capture into neutral Rydberg series converging to the vibrationally excited $X\,^2\Pi(v \geqslant 1)$ and $a\,^4\Sigma^-(v \geqslant 1)$ $NH^+$ states. The most clear feature suggesting an influence of these excitation channels on the measured DR rate coefficient is the sharp drop in $\alpha_{\rm mb}$ at $E_{\rm d} \approx 0.35$ eV (labeled by VIII). This edge matches well to the $v = 1$ levels of the $X\,^2\Pi$ and $a\,^4\Sigma^-$ $NH^+$ states. At higher energies, the upper edges of peaks X and XI may be related to $v = 2$ and $v = 3$ levels of the $X\,^2\Pi_{3/2}$ and $a\,^4\Sigma^-$ states of $NH^+$. However, between features VIII and X lies peak IX, the upper edge of which cannot be assigned to any $NH^+$ vibrational level. This feature may be due to DR resonances via doubly excited bound neutral states with electronically excited $NH^+$ cores, as is discussed in the previous paragraph. Feature VII may also have a similar origin.

Some of the structures seen in the ∼0.05 to ∼3 eV energy range also seem to be related to the opening of new final channels associated with higher excitation of the products. For example, peak IV at $E_{\rm d} \approx 0.12$ eV matches very well with the threshold for product excitation channel 4 of N and H from the $NH^+$ ground state (see Table 1). According to Goldfield & Kirby (1987) and Owono Owono et al. (2007), at least six NH states can predissociate to product excitation channel 4. Taking all possible switching between these states into account, a large number of predissociation pathways to channel 4 are available. This is to be contrasted with the more endothermic product excitation channels (5, 6, etc.), which do not show as good of a match with peaks in our experimental DR spectrum. Moreover, the existence of additional peaks between the predicted energy thresholds, such as feature IX, again suggests the existence of more complex DR pathways as discussed above.

A more general phenomenon of molecular DR, known for most species, is the increase of the DR rate above ∼4 eV with two broad peaks, XIII and XIV at $E_{\rm d} \approx 7$ eV and 10 eV, respectively (see Figure 1). These reflect direct electron capture to NH doubly excited unbound states with $2\,^2\Pi$ and $2\,^4\Sigma^-$ $NH^+$ ionic cores. In Figures 1 and 3, we label the respective vertical excitation energies for these two $NH^+$ states by D and E. We have investigated this phenomenon in more detail independently by the fragment imaging technique (Yang et al. 2014).

### 5.2. Plasma Rate Coefficient

Our experimentally derived DR plasma rate coefficient for $NH^+$ differs significantly from the currently recommended DR data. The only previous experimental investigation for DR of $NH^+$ is by McGowan et al. (1979). The results published in their original paper were later corrected for an erroneous form factor (Mitchell 1990; J. B. A. Mitchell 2012, private communication) yielding a plasma rate coefficient of $\alpha_{\rm pl}^{\rm MG} = 4.3 \times 10^{-8}(300/T_{\rm pl})^{0.5}$ cm$^3$ s$^{-1}$ with an uncertainty of ∼15%. Based on the range of collision energies covered in the experiment of McGowan et al., $\alpha_{\rm pl}^{\rm MG}$ is valid for collisional plasma temperatures between approximately 100 K and 1000 K. However, astrochemical models commonly extrapolate $\alpha_{\rm pl}^{\rm MG}$ outside this temperature range by simply following the functional expression given above. Comparing to our new results for DR of $NH^+$, we find that the magnitude of our rate coefficient is significantly larger than $\alpha_{\rm pl}^{\rm MG}$ for all values of $T_{\rm pl}$. Additionally, we see that for $T_{\rm pl} \lesssim 1000$ K our $\alpha_{\rm pl}$ decreases with increasing $T_{\rm pl}$ about 1.5 times faster than does $\alpha_{\rm pl}^{\rm MG}$. The unusual bump in our thermal rate coefficient starting at ∼1000 K and reaching a maximum at ∼4000 K originates from the cross-section enhancement at $E \approx 0.05$–3 eV. As discussed above, this can be attributed to electron capture to doubly excited states attached to electronically excited bound states of the $NH^+$ ion. Similar cross-section enhancements were observed for other

systems, such as $CH^+$ and $OH^+$ (Amitay et al. 1996a, 1996b). The corresponding high temperature increase in $\alpha_{pl}$ should thus be considered as a general DR feature, which cannot be correctly described by the hyperbolic fit functions used by the astrochemical databases. Instead a more general formula, such as Equation (6), is needed to describe $\alpha_{pl}$ for all $T_{pl}$ relevant for molecular ions.

Taking the ratio of $\alpha_{pl}/\alpha_{pl}^{MG}$ yields factors of 9.0, 5.8, 4.0, 2.8, and 2.3 at $T = 10, 30, 100, 300$, and 1000 K, respectively. These differences greatly exceed the combined experimental error bars of McGowan et al. and our present results. We attribute the differences between $\alpha_{pl}$ and $\alpha_{pl}^{MG}$ to the substantially different internal excitation of the $NH^+$ ions in the two experiments. As discussed in Section 3.2, $NH^+$ is expected to relax while stored in TSR and reach thermal equilibrium with the 300 K temperatures of the TSR chamber. Only rotational and fine-structure levels in the lowest two electronic states are expected to remain populated. On the other hand, in the single-pass merged-beams experiment of McGowan et al. the flight time from the ion source to the interaction region was $\sim$1 $\mu$s. Thus, the $NH^+$ ions are expected to have been highly excited vibrationally, rotationally, and electronically. Other experimental studies show that internal excitation of the ions may significantly affect the DR rate coefficient (e.g., Amitay et al. 1998; McCall et al. 2004).

Where no reliable DR data exist for diatomic molecules, astrochemical models commonly assume a "typical" rate coefficient of $\alpha_{pl}^{di} \approx 2.0 \times 10^{-7} \times (300/T)^{0.5}$ cm$^3$ s$^{-1}$ (Florescu-Mitchell & Mitchell 2006). As has been shown for $CF^+$ (Novotný et al. 2005) and $HCl^+$ (Novotný et al. 2013), $\alpha_{pl}^{di}$ does a poor job of matching the experimentally derived rate coefficient, $\alpha_{pl}$, both in magnitude and temperature dependence. Taking the ratio of our new DR results to that commonly assumed, we find $\alpha_{pl}/\alpha_{pl}^{di} = 1.9$, 1.2, 0.9, 0.6, and 0.5 at $T = 10, 30, 100, 300$, and 1000 K, respectively.

### 5.3. Astrochemical Implications

Although many attempts have been made to detect $NH^+$ in the ISM, none have been successful (Snow 1979; Polehampton et al. 2007; Hily-Blant et al. 2010; Persson et al. 2010, 2012; Benz et al. 2013). The nondetection of $NH^+$ at the sensitivity limits of the various observational techniques is in agreement with existing astrochemical models (e.g., Persson et al. 2010). Our new data predict that the $NH^+$ destruction by DR at $T_{pl} \lesssim 50$ K is significantly faster than previously assumed. For cold ISM environments at $T_{pl} = 10$ K this enhancement reaches a factor of between 1.9 and 9.0 depending on the $NH^+$ DR data used in the model (see Figure 4).

To estimate the relative effect of DR on the $NH^+$ abundance, we compare the two most important $NH^+$ destruction channels: DR of $NH^+$, reaction (4), and $NH^+$ reacting with $H_2$, reaction (1). Using the $NH^+ + H_2$ reaction rates from Zymak et al. (2013) and our new $NH^+$ DR data, we calculate that DR is a competitive destruction channel at electron-to-$H_2$ density ratios of $n_e/n_{H_2} \gtrsim 1.5 \times 10^{-5}$ and $\gtrsim 1.3 \times 10^{-3}$ at $T_{pl} = 10$ and 100 K, respectively. Such electron densities are predicted for diffuse and translucent interstellar clouds (Snow & McCall 2006). Our new DR data will thus result in $NH^+$ abundances significantly lower than currently predicted. As a consequence, $NH^+$ detection in the ISM is unlikely unless the current detection limits can be significantly lowered. A reduced $NH^+$ abundance will also result in lower abundances for other nitrogen hydrides produced from $NH^+$ by reactions (2) and (3). More precise quantitative predictions will require that our new $NH^+$ DR data be implemented into current gas-phase and gas–grain nitrogen chemical models of the interstellar clouds. That is, however, beyond the scope of our work.

Lastly, we note that even in our present storage ring experiment, the $NH^+$ ions are still internally excited to $T_{exc} \sim 300$ K. In the cold ISM, however, the internal excitation is expected to be significantly lower. This is because in very low density ISM environments the collision rate is much lower than the typical radiative decay time (Spitzer 1978). Thus, $T_{exc}$ is generally even lower than the kinetic temperature, $T_{pl}$, and most of the molecules are expected to be in their rotational ground state. The response of the DR rate coefficients to $T_{exc}$ have been investigated only for light ions (e.g., Amitay et al. 1996a; Zhaunerchyk et al. 2007, Petrignani et al. 2011; Schwalm et al. 2011). From these few studies, we are unable to draw predictions for $NH^+$ DR data with $T_{exc} < 300$ K. Future studies at MPIK using the currently under-construction Cryogenic Storage Ring, which will have an internal ambient temperature of $\sim$10 K, will be able to address this issue (Fadil et al. 2006; Wolf et al. 2006; Krantz et al. 2011; von Hahn et al. 2011).

## 6. SUMMARY

We have measured the absolute DR rate coefficient for $NH^+$ in a merged-beams configuration at electron-ion collision energies up to 12 eV. For astrophysical applications, we have converted the experimental merged-beams rate coefficient to a cross section and a plasma rate coefficient. The resulting plasma rate coefficient is faster compared to the DR data currently used in most astrochemical models. Using the updated $NH^+$ data we expect that the $NH^+$ abundances will become even lower than currently predicted. This is in agreement with the nondetection of $NH^+$ in interstellar clouds. Our new $NH^+$ data need to be implemented in the state-of-the-art astrochemical models for quantitative abundance predictions for nitrogen hydrides in general.

We thank the MPIK accelerator and TSR crews for their excellent support. We also thank P. Pernot for stimulating discussions concerning the error analysis. O.N. and D.W.S. were supported in part by the NSF Division of Astronomical Sciences Astronomy and Astrophysics Grants program and by the NASA Astronomy and Physics Research and Analysis Program. D.S. acknowledges the support of the Weizmann Institute of Science through the Joseph Meyerhoff program. The work is supported in part by the German-Israeli Foundation for Scientific Research (GIF under contract no. I-900-231.7/2005). W.G. acknowledges partial support by the COST Action CM0805: "The Chemical Cosmos: Understanding Chemistry in Astronomical Environments." B.Y. is thankful for support from MPG, the National Basic Research Program of China (grant No. 2010CB832901), and the Joint Funds of the National Natural Science Foundation of China (Grant No. U1332206). The work is supported in part by the DFG Priority Program 1573 "Physics of the Interstellar Medium."

## REFERENCES

Amero, J. M., & Vázquez, G. J. 2005, IJQC, 101, 396
Amitay, Z., Zajfman, D., & Forck, P. 1994, PhRvA, 50, 2304
Amitay, Z., Zajfman, D., Forck, P., et al. 1996a, PhRvA, 54, 4032
Amitay, Z., Zajfman, D., Forck, P., et al. 1996b, PhRvA, 53, 644
Amitay, Z., Baer, A., Dahan, M., et al. 1998, Sci, 281, 75
Asplund, M., Grevesse, N., Sauval, A. J., & Scott, P. 2009, ARA&A, 47, 481

Bardsley, J. N. 1968, JPhB, 1, 365
Bates, D. R. 1950, PhRv, 78, 492
Beloy, K., Kozlov, M. G., Borschevsky, A., et al. 2011, PhRvA, 83, 062514
Benz, A. O., Bruderer, S., van Dishoeck, E. F., Stäuber, P., & Wampfler, S. F. 2013, JPCA, 117, 9840
Brzozowski, J., Elander, N., Erman, P., & Lyyra, M. 1974, PhyS, 10, 241
Buhr, H., Mendes, M. B., Novotný, O., et al. 2010, PhRvA, 81, 062702
Cheng, M., Brown, J. M., Rosmus, P., et al. 2007, PhRvA, 75, 012502
Cheung, A. C., Rank, D. M., Townes, C. H., Thornton, D. D., & Welch, W. J. 1968, PhRvL, 21, 1701
Clement, S. G., Ashfold, M. N. R., Western, C. M., Johnson, R. D., & Hudgens, J. W. 1992, JChPh, 97, 7064
Colin, R. 1989, JMoSp, 136, 387
Colin, R., & Douglas, A. E. 1968, CaJPh, 46, 61
de Almeida, A. A., & Singh, P. D. 1982, A&A, 113, 199
Dislaire, V., Hily-Blant, P., Faure, A., et al. 2012, A&A, 537, 20
Fadil, H., Grieser, M., von Hahn, R., et al. 2006, in AIP Conf. Proc. 821, Beam Cooling and Related Topics, ed. S. Nagaitsev & R. J. Pasquinell (Melville, NY: AIP)
Florescu-Mitchell, A., & Mitchell, J. 2006, PhR, 430, 277
Forck, P., Broude, C., Grieser, M., et al. 1994, PhRvL, 72, 2002
Goldfield, E. M., & Kirby, K. P. 1987, JChPh, 87, 3986
Hily-Blant, P., Maret, S., Bacmann, A., et al. 2010, A&A, 521, L52
Hübers, H.-W., Evenson, K. M., Hill, C., & Brown, J. M. 2009, JChPh, 131, 034311
Kawaguchi, K., & Amano, T. 1988, JChPh, 88, 4584
Kilgus, G., Habs, D., Schwalm, D., et al. 1992, PhRvA, 46, 5730
Krantz, C., Berg, F., Blaum, K., et al. 2011, JPhCS, 300, 012010
Langer, W. D., & Graedel, T. E. 1989, ApJS, 69, 241
Larsson, M., & Orel, A. E. 2008, Dissociative Recombination of Molecular Ions (Cambridge: Cambridge Univ. Press)
Lestinsky, M. 2007, Dissertation, Universität Heidelberg, http://www.ub.uni-heidelberg.de/archiv/7334/
Lestinsky, M., Lindroth, E., Orlov, D. A., et al. 2008, PhRvL, 100, 033001
Linstrom, P., & Mallard, W. (ed.) 2013, NIST Chemistry WebBook, NIST Standard Reference Database Number 69 (Gaithersburg, MD: National Institute of Standards and Technology), 20899, http://webbook.nist.gov
Marquette, J. B., Rebrion, C., & Rowe, B. R. 1988, JChPh, 89, 2041
McCall, B. J., Huneycutt, A. J., Saykally, R. J., et al. 2004, PhRvA, 70, 052716
McElroy, D., Walsh, C., Markwick, A. J., et al. 2013, A&A, 550, 36
McGowan, J. W., Mul, P. M., D'Angelo, V. S., et al. 1979, PhRvL, 42, 373
Meyer, D. M., & Roth, K. C. 1991, ApJL, 376, L49
Mitchell, J. B. A. 1990, PhR, 186, 215
Novotný, O., Badnell, N. R., Bernhardt, D., et al. 2012, ApJ, 753, 57
Novotný, O., Becker, A., Buhr, H., et al. 2013, ApJ, 777, 54
Novotný, O., Mitchell, J. B. A., LeGarrec, J. L., et al. 2005, JPhB, 38, 1471
Novotný, O., Motapon, O., Berg, M. H., et al. 2009, JPhCS, 192, 012021
Orlov, D. A., Krantz, C., Wolf, A., et al. 2009, JAP, 106, 054907
Orlov, D. A., Weigel, U., Schwalm, D., Terekhov, A. S., & Wolf, A. 2004, NIMPA, 532, 418
Owono Owono, L. C., Jaidane, N., Kwato Njock, M. G., & Ben Lakhdar, Z. 2007, JChPh, 126, 244302
Padellec, A. L., Mitchell, J. B. A., Al-Khalili, A., et al. 1999, JChPh, 110, 890
Palmieri, P., Tarroni, R., & Amos, R. D. 1996, JPhCh, 100, 6958
Persson, C. M., Black, J. H., Cernicharo, J., et al. 2010, A&A, 521, L45
Persson, C. M., De Luca, M., Mookerjea, B., et al. 2012, A&A, 543, A145
Peterson, J. R., Padellec, A. L., Danared, H., et al. 1998, JChPh, 108, 1978
Petrignani, A., Altevogt, S., Berg, M. H., et al. 2011, PhRvA, 83, 032711
Pickles, J. B., & Williams, D. A. 1977, Ap&SS, 52, 453
Polehampton, E. T., Baluteau, J.-P., Swinyard, B. M., et al. 2007, MNRAS, 377, 1122
Poth, H. 1990, PhR, 196, 135
Ralchenko, Y., Kramida, A., Reader, J., & NIST ASD Team. 2011, Atomic Spectra Database, version 4.1.0, http://physics.nist.gov/asd (Gaithersburg, MD: National Institute of Standards and Technology)
Schwalm, D., Shafir, D., Novotny, S., et al. 2011, JPhCS, 300, 012006
Shafir, D., Novotny, S., Buhr, H., et al. 2009, PhRvL, 102, 223202
Snow, T. P. 1979, Ap&SS, 66, 453
Snow, T. P., & McCall, B. J. 2006, ARA&A, 44, 367
Spitzer, L. 1978, Physical Processes in the Interstellar Medium (New York: Wiley)
Sprenger, F., Lestinsky, M., Orlov, D. A., Schwalm, D., & Wolf, A. 2004, NIMPA, 532, 298
Steck, M., Bisoffi, G., Blum, M., et al. 1990, NIMPA, 287, 324
Tanabe, T., Katayama, I. S. O., et al. 1998, JPhB, 31, L297
Unser, K. 1981, ITNS, 28, 2344
van Dishoeck, E. F., Jansen, D. J., Schilke, P., & Phillips, T. G. 1993, ApJL, 416, L83
von Hahn, R., Berg, F., Blaum, K., et al. 2011, NIMPB, 269, 2871
Vuitton, V., Yelle, R. V., & Anicich, V. G. 2006, ApJL, 647, L175
Wakelam, V. 2010, in SF2A-2010: Proceedings of the Annual Meeting of the French Society of Astronomy and Astrophysics, ed. S. Boissier, M. Heydari-Malayeri, R. Samadi, & D. Valls-Gabaud (Marseilles, France: SF2A), 239
Wakelam, V., Herbst, E., Loison, J.-C., et al. 2012, ApJS, 199, 21
Wilson, I. D. L., & Richards, W. G. 1978, Natur, 271, 137
Wolf, A. 1999, in Atomic Physics with Heavy Ions, ed. H. F. Beyer & V. P. Shevelvo (Berlin: Springer), 1
Wolf, A., Buhr, H., & Novotný, O. 2011, JPhCS, 300, 012008
Wolf, A., von Hahn, R., Grieser, M., et al. 2006, in AIP Conf. Proc. 821, Beam Cooling and Related Topics, ed. S. Nagaitsev & R. J. Pasquinelli (Melville, NY: AIP)
Woon, D. E. 2012, http://www.astrochymist.org/astrochymist_ism.html
Wyckoff, S., Tegler, S. C., & Engel, L. 1991, ApJ, 367, 641
Yang, B., Novotný, O., Krantz, C., et al. 2014, JPhB, 47, 035201
Zhaunerchyk, V., Al-Khalili, A., Thomas, R. D., et al. 2007, PhRvL, 99, 013201
Zymak, I., Hejduk, M., Mulin, D., et al. 2013, ApJ, 768, 86